

Deep Hyperspectral Shots: Deep Snap Smooth Wavelet Convolutional Neural Network Shots Ensemble for Hyperspectral Image Classification

Farhan Ullah, Yaqian Long, Irfan Ullah, Rehan Ullah Khan, Salabat Khan, Khalil Khan, Maqbool Khan, Giovanni Pau

Abstract—The deployment of Convolutional Neural Networks to classify hyperspectral images is extensively discussed in the research study. A number of different algorithms and approaches are applied, including 2D CNN, 3D CNN, SVM, Regression models, and other state-of-the-art deep learning models, though these methods do not show good performance for hyperspectral image classification. Furthermore, 3D CNNs require a lot of computational power and are not mainly employed, whereas 2D CNNs do not constitute multi-resolution image processing and exclusively focus on spatial features. However, 3D-2D CNNs aim to incorporate spectral and spatial features, their efficiency while being evaluated on various datasets tends to be limited. Moreover, a number of deep learning models have been proposed recently, but their performance is still limited. In order to solve these problems, in this article, we propose a novel Deep Hyperspectral Shots, a deep smooth wavelet convolutional neural network shots ensemble for hyperspectral image classification. A deep smooth wavelet convolutional neural network utilizes layers of wavelet transform to extract spectral features. The computation of a wavelet transform is less intensive as compared to the computation of a 3D CNN. After that, the extracted spectral features are integrated into 2D CNN, which generates spatial features, as a result, generates a spatial-spectral feature vector for classification. Furthermore, we introduce the snapshots generation method and employ Cyclic Annealing Schedule (CAS) to converge to several local minima along its optimization path and save the models. We build several snapshots of the Deep Hyperspectral Shots model to enhance the performance of our proposed method. We propose the snapshots optimization and ensemble selection approach in order to solve the optimization problem within ensemble creation and further enhance the performance. In addition, we also introduce a novel activation function called Relish to increase spatial-spectral feature propagation and advance for smoother gradients. Overall, we ensemble the snapshots of our proposed method and achieved that can classify multi-resolution HSI data with high accuracy. Experiments performed on benchmark datasets, our proposed method Deep Hyperspectral Shots achieved overall accuracies (OAs) of

99.96%, 97.91%, and 99.49% on the Salinas, Indian Pines and Pavia University datasets against the state-of-the-art methods.

Index Terms—Hyperspectral Image Classification, Snapshot, Wavelet Convolutional Neural Network, Deep Learning, Ensemble.

I. INTRODUCTION

HYPERSPECTRAL images (HSIs) have received a lot of focus in current years, because of the valuable features and high spectral resolution [1], [2]. Using these comprehensive hyperspectral image data, HSIs are used effectively in a variety of application domains, some examples of applications are including urban development, land monitoring, scene interpretation, and resource exploration [3]–[6]. For these applications, Hyperspectral Image Classification (HSIC) is a popular approach that provides the opportunity for the analysis of earth feature properties, thus also making it easier for HSI applications.

Over the last several decades, a large number of classification techniques based on spectral and spatial characteristics have been developed to classify the pixels in HSI dataset, those techniques are incorporating Support Vector Machines (SVMs) [7] [8] K-Nearest Neighbors (KNN) [9], Random Forest (RF) [10], Logistic Regression (LR) [11], Extreme Learning Machine (ELM) [12], and deep learning models, etc. Nevertheless, as such techniques consider pixel values with very related spectral data but not the same label, the classification performance is often limited, because the leverage of spatial information is rarely taken into consideration. Following that, a number of techniques have used spatial characteristics as a secondary approach, based on spectral characteristics, to improve the illustration of hyperspectral data. For example, the fine-tuned classification maps generated by SVMs, Markov Random Field (MRF), and edge-preserving filtering are employed to accept spatial contextual data into account [13], [14]. Morphological profiles [15]–[17] have been advanced to transform the spatial feature extraction of high dimensional hyperspectral data, which has been proven to be an effective method to analyze spatial data. In [18], [19], the spatial data of each pixel's neighborhood is presented to a sparse representation model in order to find the best representation approach using a sequence of standard training instances. Moreover, diverse image processing techniques, for instance, Gabor Filtering (GF) [20], compressive sensing [21], and discriminant analysis [22], [23], are also

Corresponding author: Giovanni Pau

Farhan Ullah, Yaqian Long, and Salabat Khan are with the College of Computer Science and Software Engineering, Shenzhen University, Shenzhen 518060, China (farhan.marwat@gmail.com; longyaqian@szu.edu.cn; salabat-wazir@gmail.com)

Irfan Ullah is with the School of Computer Science, Chengdu University of Technology, Sichuan, China (irfan.ee@cqu.edu.cn)

Rehan Ullah khan is with the Department of Information Technology, College of Computer, Qassim University, Buraydah, Saudi Arabia (rehan-marwat1@gmail.com)

Khalil Khan is with the Department of computer science, Nazarbayev university Kazakhstan (khalil.khan@nu.edu.kz)

Maqbool Khan is with the Pak-Austria Fachhochschule Institute of Applied Sciences and Technology, Haripur, Pakistan (maqbool@163.com)

Giovanni Pau is with the Kore University of Enna, Italy (giovanni.pau@unikore.it)

employed for HIC with the add-on of spectral and spatial information.

Despite the fact that the above-mentioned techniques have yielded appropriate results, the validity of their classification is largely relying on the reliability of the hand-crafted features, which are regarded as superficial features. The experiments of the aforesaid shallow models are vulnerable to overfitting problems due to the Hughes Phenomenon (HP) [24] and the smaller sample size. Furthermore, due to erratic environmental forces, there is commonly severe spectral diversity in HSI, resulting in a massive intra-class distance and intense inter-class correlation. Therefore, hand-crafted patterns are not suitable for dealing with these issues. The extraction of dynamic spectral and spatial characteristics for HSIC is a commonly known commercial need in the associated industry.

Deep Learning (DL) has experienced significant growth with the growing scalability of hardware, DL has experienced significant growth in Computer Vision (CV) tasks (e.g., image classification [25]–[27], scene segmentation [28], target detection [29], and Natural Language Processing (NLP) [30], [31]), etc. A number of DL-based algorithms have been proposed to compute the HSIC datasets, which can be further classified into two types, i.e. spectral-based technique, and spectral-spatial-based technique, based on the method of data processing. The spectral-based techniques exclusively employ spectral data, e.g., to explore the subtle spectral disparities among various classes, a high-dimensionality spectrum was fed into a Deep Neural Network (DNN) [32]. Rather than computing each band separately, a Recurrent Neural Network (RNN), was employed to maximize the utilization of the spectral similarity that occurs in the specific bands [33]. To reduce the computational complexity of overlapping data between adjacent bands and improve classification performance, a cascaded RNN approach with two RNN layers was presented, whereas one intends to minimize concurrency and another to learn complementarity [34]. Gradients could come to a halt throughout the RNN training process due to the trait of long-term reliance. Hence, Long Short-Term Memory (LSTM) networks, a novel model of RNN, are introduced to obtain the context-specific spectral features efficiently to address this gap [35], [36]. However, such spectral-based techniques have enhanced classification performance, and their efficiency in complex scenes still needs to be improved.

Unlike the previously mentioned, spectral-spatial-based techniques intend to retrieve both spectral and spatial features for classification performance concurrently. Numerous pieces of research have been performed on this concept so far. In another study the author employed [37], Principal Component Analysis (PCA) to reduce the high-dimensionality of the HSI datasets, then every pixel and the flattened vector of the correlating neighbors were fed into the multi-layer stacked auto-encoders to retrieve spectral-spatial features. In the course of feature learning, the authors itema2016spectral36 introduced a spatially updated deep auto-encoder that considered contextual meta-data to achieve maximum inter-class distances. Deep Belief Networks (DBNs) were also used in order to acquire representative spectral features and score neighboring pixels' estimates [38], [39]. Even so, these approaches primarily infuse

spatial input data into flat vectors, that can suppress spatial structure.

Convolutional Neural Networks (CNNs) have illustrated the potential of extracting features and influenced the research area of HIS Classification tasks due to the distinctive potential benefits of general perception and parameter tuning. The basic two categories of CNN architectures, such as 1-D CNN and 2-D CNN, were constructed to acquire the robust spectral-spatial features, and subsequently successfully obtain the classification result through the decision fusion approaches [40]–[42]. Moreover to acquire robust spectral-spatial features, an HSI cubes that include the central pixels and its neighbor pixels was chosen as the training instance of a DNN. Due to the sheer intense spectral correlation among the Centre pixels and the neighbouring pixels in a limited area, such a method suggests that the label of the whole HSI cube can be illustrated via the label of the central pixel. According to this supposition, 3-D has been the best suitable Deep Learning architecture for extracting spectral-spatial features [42]. Furthermore, the Jeffries-Matusita distance was combined with 3-D CNN to adopt efficient bands for the classification of distinct closely related objects [43]. To tackle the problems of significant hyper-parameters and extreme time complexity of the training model, such 3-D convolutional layers at depth levels are replaced via employing 2-D convolutional layers to efficaciously optimize deep neural networks and integrate features at various levels [44], [45].

The general perspective of a Deep Neural Network (DNN) is, the more the Deeper the architecture of a DNN, the more efficient and related the features are extracted. However, the depth of the DNN levels may lead to a vanishing gradient problem. In order to address this issue, a residual network (ResNet) was introduced, which uses shortcut connections in residual blocks to achieve instantaneously gradient propagation from higher layers to lower layers [46]. Zhong et al. [47] To alleviate the decreasing-accuracy problem, a deep spectral-spatial ResNet was proposed with a serial residual blocks. In [48], presented a pyramid bottleneck residual block to incorporate extra feature map locations in the deeper network. In [49], the authors integrated the spectral-spatial Fractal Residual CNN (FRCNN). Moreover, to solve the issue of limited labeled data they integrate of data balance augmentation approach to enhance the accuracy of the limited samples size. Furthermore, a Dual-Channel Residual Network (DCRN) with a noise-robust loss function was presented to thoroughly exploit the valuable data from incorrectly labeled samples to improve the DNN model effectiveness in unique scenes [50]. Due to the previously significant research progress, ResNet has become the dominant architectural style of spectral-spatial-based techniques for HSI classification.

Nevertheless, there is one typical major downside that has yet to be addressed. HSI generally carries a wide range of spectral and spatial details, though not all of it is useful for classification [51]. Moreover, the spectral bands and salient spatial locations that are useful for feature representation and classification should be illustrated. In order to achieve this, the attention method has been successfully applied to natural language translation [52] and CV tasks [53], [54] have also been

proposed to detect the majority of salient bands and locations in HSIs. Among application areas, the attention method is typically integrated as an individual block in networks to improve feature maps by unevenly weighting bands, pixels, or channels. E.g., In the initial phases, light-weight spectral attention blocks constructed of Global Average Pooling (GAP) layers and convolutional layers were introduced at the top of the networks to enhance the impactful spectral bands to perform the main function in resulting feature extraction [55], [56].

In addition to the spectral attention block, the spatial attention block was intended to increase the importance of the related spatial regions. In [57], e.g., used spatial attention to improve the network's generalization capacity during feature fusion. In a sequential manner integrating the spectral and spatial attention blocks into the residual connections, effective spectral-spatial features are calculated to enhance classification of overall majority outputs [51], [58]–[60]. Nevertheless, in the aforementioned techniques, the spectral and spatial attention blocks are generated individually, preventing the fusion of spectral and spatial properties. To enhance the association between spectral and spatial attentions, similarity matrices produced by the spectral and spatial attention sections were dynamically assigned to all locations and bands [61]. Li et al [62] introduced a spectral and spatial fused attention block to cross-apply attention masks, intending to thoroughly explore the significant association between spectral bands, spatial locations, neighborhoods, and classification outcomes. Furthermore, self-attention (SA) was used to analyse the associations among pixels. A SA methodology was developed in order to retrieve distinguishing spectral and spatial features [63]. The authors in [64], presented an approach to calculate the correlation coefficients between the center pixel and its neighbors to improve the impact of the center pixel. The spectral and spatial transformers [65], [66] were used to predict the correlation between spectral bands and spatial positions by incorporating various SA components. In addition, the transformer was used to acquire the enhanced inputs for computation [67]. Even so, the computational complexity is immense because the transformer typically contains multiple SA modules.

In [68] and [69], the spectral and spatial nonlocal blocks retrieve the global salient spectral bands and spatial areas. Both are integrated with the spectral and spatial blocks, respectively, to optimize the features. Recently, Graph Convolutional Neural Network (GCNN) [70] has been proposed to extract similar features from the spatial and spectral features of HSI and improve the performance issue of HSIC. Many spatial-spectral proposed hybrid methods [71]–[73] have been developed by combining spatial correlations and spectral similarity [74], by connecting the integrated correlations and spectral similarity of nearby pixels, a spatial-spectral hypergraph was created within the class. The authors in [75] proposed a new multireceptive field-based neural (MARF) method for HSIC. In this method A novel approach called the adaptive receptive path aggregation (ARP) mechanism is introduced to mitigate the influence of noise nodes on classification. This mechanism also enables the automatic exploration of an adaptable receptive field. To achieve this, a graph attention (GAT) neural network is

utilized to learn the significance of neighborhoods with varying sizes. Additionally, the method involves the integration of a LSTM technique to update nodes and retain the inherent local convolutional features of these nodes. Similarly In [76], the authors proposed a novel multi-scale receptive fields graph attention neural network (MRGAT) for HSI. In [77], an adaptive graph convolution approach termed (AF2GNN) is introduced for HSIC. It incorporates superpixel segmentation to refine local spatial features, and a two-layer 1D CNN for spectral feature transformation. A linear function combines various graph filters through learned weight matrices. Furthermore, degree-scalers unify multiple filters, outlining the graph structure. The AF2GNN network integrates adaptive filters and aggregator fusion, enabling comprehensive HSIC. In [78], the authors introduced a new approach named spectral-induced aligned superpixel segmentation, which simultaneously employs segmentation outcomes from raw and deeply abstracted spectral features in HSI. Deep spectral features are extracted through a deep autoencoder. Minimum and maximum fusion approaches are intuitively examined to combine these segmentation results. Additionally, they introduce a Local Aggregation and Global Attention Block (LAGAB), integrating graph sampling, aggregation, and graph transformer to hierarchically examine local and global spatial characteristics. The aforementioned methods typically retrieve spatial features based on coordinate distance, which prevents them from capturing key features. Additionally, the majority of them only take these spatial features into account when pre-processing the HSI data and do not take them into account when building the graph [79], [80]. Furthermore, the aforementioned techniques are built on a solo graph structure to guide the weak diversity learning of intrinsic properties found in HSI data. In order to alleviate the phenomenon, ensemble learning [81], [82] draws much attention. However, the existing ensemble learning algorithms are prone to computational complexity problems.

Although notable significant progress has been made in the research area of spectral-spatial HSIC technique, it remains crucial to improve discriminative features and performance in contexts of accuracy prospects. In this paper, we proposed Deep Hyperspectral Shots, which are presented to characterize the spatial and spectral features of HSIC. The proposed method's goal is to be capable to develop discriminative representations for spectral and spatial characteristics, as well as to improve the robustness of features through embedded learning via dense concatenation, Snapshots, and ensemble learning. To accomplish the aforementioned task, we build four distinct parts in the proposed Deep Hyperspectral Shots architecture. Firstly, to efficiently compute the feature extraction and reduce the time complexity issue, Factor Analysis and wavelet decomposition methods have been employed, which reduces the training and time complexity issue efficiently to exploit the CNN. Secondly, the excessively dense features emphasize the overfitting and redundancy issues, which reduce classification performance as the number of dense features increases. Recently, the Ensemble approach has been extensively applied to a variety of tasks, such as CV, NLP, [83], [84], which is motivated by the human team task efficiency. Motivated by the fact that the Snapshot ensembling can improve representation discrimination

and help improve the time complexity generally associated with Ensemble approach creation. Moreover, we proposed a Snapshot selection technique to optimize the Ensemble approach and efficiently compute the spatial and spectral features of HSI. In this paper, the 2D and 3D spatial and spectral modules are built individually to yield productive feature representation. Third, in order to enhance the performance and low computation complexity problem, we design an improved activation function. Finally, to further extract the dense feature of HSI for classification, and performance enhancement on spatial and spectral features diversified data set, which aims to optimize more plausible data and help boost classification accuracy.

This article's key contributions are described as follows.

- 1) We propose the Deep Hyperspectral Shots method which extracts the spatial and spectral features efficiently. Moreover, we proposed the Snapshot ensemble approach to enhance the performance.
- 2) We incorporate the novel Snapshots optimization and ensemble selection approach to obtain additional accurate classification performance.
- 3) We also introduce a novel Relish activation function that has been integrated into the proposed method to boost spatial-spectral feature propagation and advance for smoother gradients. This tends to make the landscape simpler to optimize, allowing for smoother and faster generalization of the proposed method.
- 4) An end-to-end Deep hyperspectral method, which incorporates the Snapshot, the ensemble, and Deep Hyperspectral Shots is proposed to stress the relevant spatial areas and extract the discriminating spectral-spatial features for HSI classification.
- 5) A number of experiments were carried out on real-world datasets to evaluate the efficacy of our proposed method and compare it to existing methods. Experimental performance exhibit that our proposed method not only obtains enhanced performance but also can efficiently extract spectral-spatial features.

The remainder of this article is organized as follows. Section II introduces the proposed Deep Hyperspectral Shots method in a comprehensive manner. Section III presents the experiment and results analysis of three standard HSIC datasets. Finally, this article is concluded in Section IV.

II. PROPOSED METHODOLOGY

In this section, the overview of the proposed Deep Hyperspectral Shots architecture is first introduced. Then, the key parts of the framework are described comprehensively. Finally, the activation function of the network and the algorithm's steps are described subsequently.

A. Architecture

As exhibited in Fig. 1, the Deep Hyperspectral Shots architecture is a multi-snapshot ensemble feed forward neural network that consists of five explicit functional parts, such as the Pre-processing part, the base or core model, Snapshots Generation, Snapshot optimization and ensemble selection,

and finally the output part. From the forward propagation process, the output of every individual Snapshot is utilized as the output of the core model generation. For example, we employ core-model to produce several Snapshots required by the Deep Hyperspectral Shots and final output part. The Snapshot optimization and ensemble selection approach is applied for the fusion part to train the acquired spectral and spatial features.

The basic notation of each part in Fig. 1 are described as follows: The orange rectangle box indicates the base/core model which includes the pre-processing part which converts the original map into low-dimensional features, the middle part contains the contains all neuron of the Deep Hyperspectral Snapshots and Wavelet Transform framework. The black line of the core model indicates the activate function infuse through a core model. The purple lines are the Snapshots generation process. The blue boxes show the Snapshots from $1, \dots, 1 + n$, generated by a core model. The red vertical rectangle box is the Snapshot optimization and ensemble selection procedure to optimize the Snapshots and generate a prediction for the final output of the proposed method. The following operational parts will be thoroughly discussed below.

B. Feature Extractions

In order to enhance computational efficacy, the input HSI cube with dimension $P \times Q \times R$ is initially forwarded to a Factor Analysis (FA) technique to minimize the dimension to $P \times Q \times B$. Minimizing the dimension of the original HSI cube helps in decreasing the overall training time complexity by 60% [85]. The output vector \tilde{Y} , with a dimension of $1 \times PQ$, selects one of the accessible land cover classes defined by C . The spectral dimensions are saved in FA, i.e., $P \times Q$, only the bands are scaled down from R to B . Using FA as a pre-processing phase in HSI is immensely effective because it can characterize the variations among the distinct correlated and intersecting spectrum bands, allowing the model to effectively classify related instances. However, the frequently utilized PCA-based dimension reduction does not thoroughly focus on this goal in HSI. PCA generates an approximate value for the desired factors, but it does not enable categorizing resembling instances very efficiently. Following the completion of the FA phase, intersecting 3D patches of size $F \times F \times B$ are retrieved from the pre-processed HSI and issued to the core model of the Deep Hyperspectral shots. $F \times F$ is the window size for patch extraction, for the Indian Pines dataset, University of Pavia, and Salinas Scene dataset, the window size has been set at 24×24 . The truth scores for the above patches are measured by the class category of the central pixel. The scores were assigned through experimental work in order to optimize overall accuracy.

C. Deep Smooth Wavelet Convolution Neural Network

The traditional two-dimensional Convolutional Neural Network (2-D CNN) can be stated as a variant of a multi-resolution CNN, which can take spatial and spectral information into account [86]. Past studies have been effective in proposing the convolution and pooling functions in a 2D CNN as

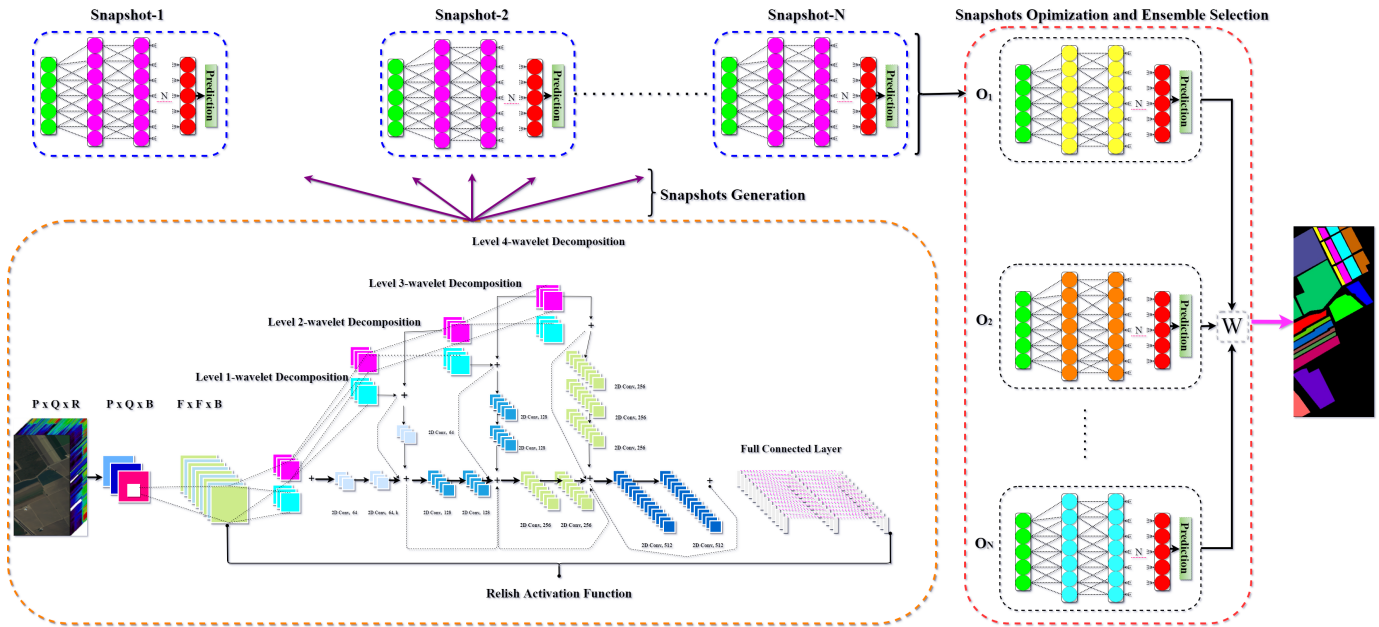


Fig. 1 Illustrates the Deep Hyperspectral Shots architecture. The orange rectangle box is consist of the base model, the blue boxes exhibit the generated Snapshots of the base model, the vertical red rectangle box consists of the Snapshots optimization and Selection process, and the final part is the output of the proposed method. (Please use the zoom-in option to explore the figure.)

filtering and down-sampling [87]. The conventional CNN can be mathematically expressed as the weighted sum of nearest neighbors with the addition of constant bias.

Given an input vector X_n with corresponding labels Y_n from the R^n space. In equation 1, Y_i is a label from Y_n labels and X_i is the corresponding sample from X_n . W_j is the weight defined by a filtering kernel. N_i are neighbouring i data.

$$y_i = \sum_{j \in N_i} W_j X_j \quad (1)$$

Equation 1 can be merely termed as the convolution of X_i and kernel W_j and can be expressed as $Y = X * W$. This is called the convolution layer of a CNN, where W is in R^o . Convolution layers output is usually huge and must be pooled down prior to being fed to the following layer. Pooling layers are incorporated in between convolution layers to initiate a filtering process and reduce the total amount of outputs. This forms the foundation for the multi-resolution CNN where the convolution is executed by a pair of kernels k_{low} and k_{high} which generate X_{low} and X_{high} . The multi-resolution CNN performs the hierarchical decomposition of the $X_{(low,t)}$ into $X_{(low,t+1)}$ and $X_{(high,t+1)}$ with different kernels at each step.

For Deep Hyperspectral Shots, we utilized the wavelet transform. The wavelet kernel $K_{high,t}$ is Haar wavelets and $K_{low,t}$ is a scaling function [88]. The two-dimensional haar wavelets employ the four kernels (fv, vfv, ufu, vfu, u) for the wavelet transform [89] as given in the equation.

$$f_{v,v} = \begin{bmatrix} 1 & 1 \\ 1 & 1 \end{bmatrix} f_{v,u} = \begin{bmatrix} -1 & -1 \\ 1 & 1 \end{bmatrix} \quad (2)$$

$$f_{u,v} = \begin{bmatrix} -1 & 1 \\ -1 & 1 \end{bmatrix} f_{u,u} = \begin{bmatrix} 1 & -1 \\ -1 & 1 \end{bmatrix}$$

After passing patch x with $F \times F$ dimensions via a Haar transform the (i_v, j_v) -th spectrum position value can be expressed as Haar:

$$(i_v, j_v) = x(2i_v - 1, 2j_v - 1) + x(2i_v - 1, 2j_v) + x(2i_v, 2j_v - 1) + x(2i_v, 2j_v). \quad (3)$$

The wavelet transform transforms the HSI patch that has been obtained as an input into sub-bands, which are then forwarded through a convolution layer to learn the spectral and location features. Please note that the sub-bands designated as high pass and low pass filters do not essentially filter the spectral band with these filters. The wavelet transform subdivides the sub-band portion once more in the following layer before sending it to the convolution layer. This procedure is repeated in each layer, with the CNN continuing to learn spectral and spatial features from the HSI patch.

The base model of the proposed method architecture is shown in Fig. 1. The model is initialized with 3x3 convolution kernels and 1x1 padding. To replace pooling layers in between convolution a stride of 2 has been employed. In order to avoid the model over-fitting issue, a global mean pooling has been used for all convolution layers before passing data into the dense layer. Furthermore, to make better use of the wavelet transformed feature, dense connections and projection

shortcuts approach have been adopted [90], [91]. To ensure that all the features stream through to the end of the model, dense connections are used with a channel-wise concatenation of the decomposed data. The base model is embedded with two dropout layers as well along with batch normalization to eliminate the over-fitting issue. Due to the small number of samples in HSI datasets, there is a high likelihood of an over-fitting. It is imperative to take every precaution to keep the base model from the over-fitting problem. Relish has been employed as the smooth activation function, the proposed activation function has been explained in detail in sub-section G.

D. Snapshot Generation

From a singular training phase, Deep Hyperspectral Shots generates ensemble of accurate and vibrant Snapshots models. An optimization technique is the core of the Deep Hyperspectral shot, which explores multiple local minima until settling on an optimum minima. In order to achieve the maximum advantage, at the training phase, we choose model Snapshots at multiple different minima.

Generally, Deep Hyperspectral Shots perform efficiently if the Snapshot models, firstly have low test error and secondly, do not overlap in the set of examples they misclassify. The weight assignments of a neural network do not always correlate to low test inaccuracy across the optimization curve. In addition, it is frequently observed that the validation loss of the Deep Hyperspectral Shots ensemble gradually declines only after the learning rate is lower, where it occurs after several hundred epochs. During our analysis, the training of our proposed method Snapshots ensemble for very lesser epochs and dropping the learning rate earlier has a slight effect on the end test error [92]. This appears to imply that local minima across the optimization curve indeed be convincing (in aspects of prediction error) only after a couple of fewer epochs.

E. Schedule Selection

We employ a Cyclic Annealing Schedule (CAS) to converge to numerous local minima as [92]. We minimize the learning rate rapidly, letting the model converge to its initial local minima in as little as 50 epochs. The optimization process is then repeated at a slightly large learning rate, perturbing the model and causing it to escape from the minimum. This procedure is reiterated numerous times in order to achieve various convergences. The learning rate is expressed in mathematical terms as:

$$\alpha(\hat{r}) = f(\text{mod}(\hat{r} - 1, \lceil N/N_i \rceil)) \quad (4)$$

where \hat{r} denotes the number of iterations, N represents the cumulative number of training iterations, and f denotes a constant declining function. Specifically, we partition the training phase into M cycles, each of which begins with a high learning rate and gradually reduces to a lower rate. The high learning rate $\alpha = f(0)$ allows the model to detach from a critical point, whereas the low learning rate $\alpha = f(\lceil N/N_i \rceil)$ leads to an effective local minimum. In our experimental studies, we initialize f to be the shifted cosine function:

$$\alpha(\hat{r}) = \frac{\alpha_0}{2} \left(\cos \left(\frac{\pi \text{mod}(\hat{r} - 1, \lceil N/N_i \rceil)}{\lceil N/N_i \rceil} \right) + 1 \right) \quad (5)$$

where α_0 is the initial learning rate. Implicitly, this function anneals the learning rate from its initial value α_0 to $f(\lceil N/N_i \rceil) \approx 0$ over the duration of a cycle. However after that, instead of updating the learning rate at each epoch, we update it at each iteration. This helps to enhance the convergence of short cycles even since a high early learning rate is chosen.

The proposed Deep Hyperspectral Shots model appears to approach a local minimum in terms of training loss at the end of each training cycle. As a result, leading up to increasing the learning rate, we start taking a "Snapshot" of the proposed model weights. After training M cycles, we have M model Snapshots, $\mathcal{O}_1, \dots, \mathcal{O}_M$, sequentially every Snapshot will be incorporated into the final ensemble. It is worth noting that the entire training time of the M snapshots is constant as training a model on a typical schedule. In certain situations, the basic learning rate schedule generates lower training loss as compared to the cyclic schedule. The algorithmic details of the proposed method are given in algorithm 1.

Algorithm 1 Snapshots Generation and Schedule Selection

Require: \mathbf{Z} : Hyperspectral images data; \mathbf{N} : total number of classes; \mathbf{M} : total number of training samples; \mathbf{L} : Snapshot; **SCB**: Snapshot Callback; **epc**: epoch per cycle; n_epoch : total number of epochs of each cycle.

- 1: **Procedure**
 - 2: Apply FA to execute the dimensionality reduction process for \mathbf{N} of HSI datasets \mathbf{Z}
 - 3: Obtain the training samples \mathbf{M} by arbitrary selection \mathbf{N} pixels from the spectral-spatial dataset \mathbf{Z} , generate the testing samples \mathbf{MT} by the remaining pixels
 - 4: Retrieve the spatial features from the hyperspectral images datasets \mathbf{Z} and acquire the spectral-spatial fusion information by using the wavelet transform method
 - 5: **for** CallBack = **SCB** **do**:
 - 6: initialize \mathbf{L}
 - 7: Execute above Equation (4), and (5)
 - 8: after each iteration n_epoch save learning rate
 - 9: **if** epoch $\neq 0$ & (epoch+1) % **epc** == 0: **do**:
 - 10: Generate and Save train \mathbf{L} model.
 - 11: **end if**
 - 12: **end for**
-

F. Snapshots Optimization and Ensemble Selection

The Snapshot selection plays a key role in the construction of a robust and enhanced performance ensemble in our proposed method. Generally, the basic approach of ensemble creation is to integrate the total number of base models by using the bagging [93], boosting [94], and stacking [95], approaches. Although our proposed method can acquire fairly good performance, we take further steps to optimize and minimize the loss in order to acquire the robust and enhanced generalized performance

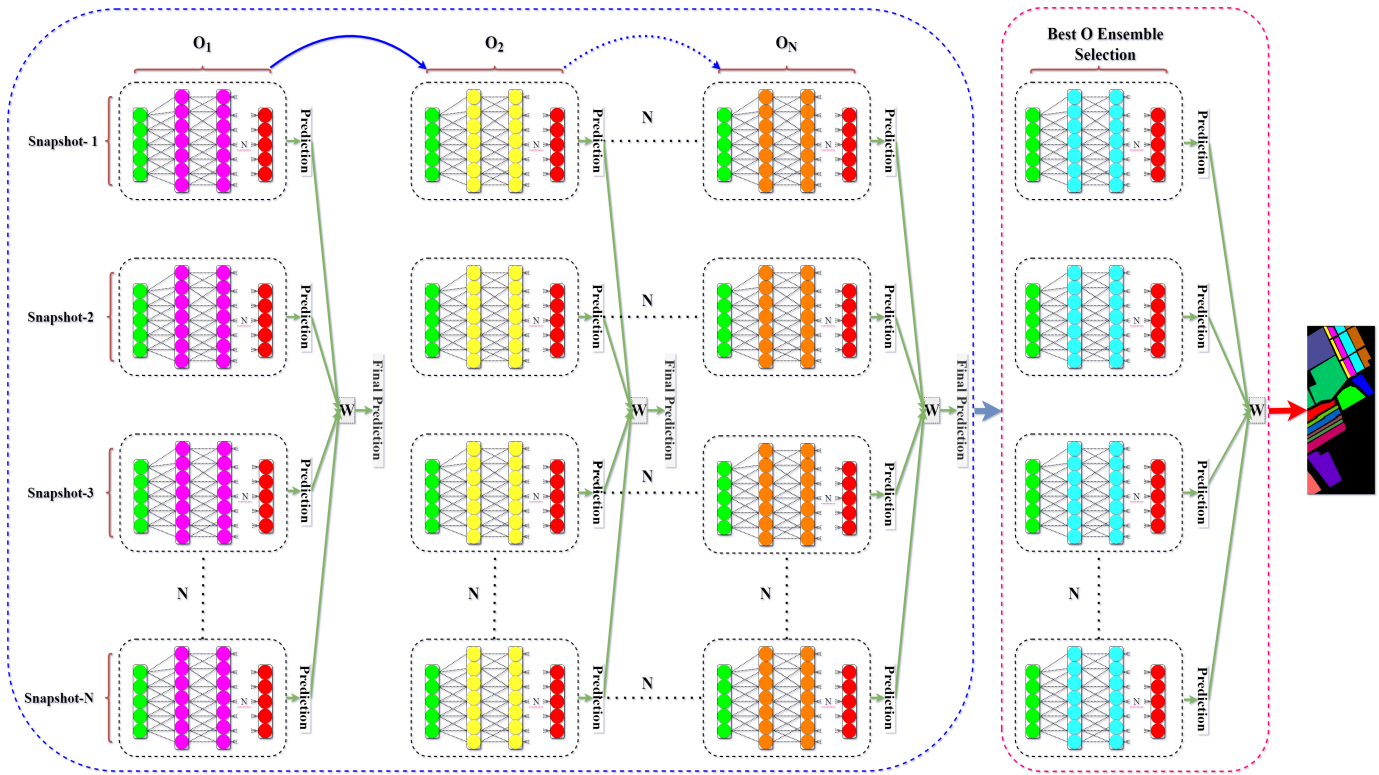


Fig. 2 Shows the Snapshots Optimization and Ensemble Selection process. The Blue box shows the optimization of T Snapshots and the red box shows the best ensemble selection and Prediction.

of the ensemble. Since we are considering a Non-Linear Programming (NLP) problem, we employ the Sequential Least Square Programming (SQLSP) approach to solve this issue. Optimizing O the Snapshots and selecting the best ensemble to allow us to further slightly enhance the performance by using the equations as:

$$\begin{aligned} \min f(q), \text{ over } q \in R^n \\ \text{subject to } k(q) = 0 \\ l(q) \leq 0 \end{aligned} \quad (6)$$

where $f: R^n \rightarrow R$ is an objective function, function $k: R^n \rightarrow R^m$ and $l: R^n \rightarrow R^z$ describe the equality and inequality constraints, n denotes the total number of variables that are subject to optimization, m is the number of equality, and z is the number of inequality constraints function. For an assigned iterative process $q[p]$, the NLP is scaled down to the QP subproblems, and the following iteration $q[p+1]$, is then derived from the QP solution. The sequence $q[p]$ is designed in such a format that it eventually converges to a local minima $f(q^*)$ of the NLP as $q \rightarrow \infty$, where $*$ relates to the parameter associated with the local minimum point. The evaluation and execution of NLP become further challenging in the existence of constraints. The values that fulfill equality and inequality constraints are referred to as the NLP's viable set and are described by:

$$\mathcal{F} = \{q \in R^n \mid k(q) = 0, g(q) \leq 0\} \quad (7)$$

The Lagrangian for this problem is

$$\mathcal{L}(q, \lambda, \mu) = f(q) + \lambda^T k(q) + \mu^T l(q) \quad (8)$$

where vectors $\lambda \in R^m$ and $\mu \in R^z$ are referred to as Lagrangian multipliers. Active constraints are an index set for $q \in R^n$ when

$$\mathcal{I}_{ac} = \{i \in \{1, \dots, z\} \mid l_i(q) = 0\} \quad (9)$$

Let $f(q^*)$ be a local minimum of the NLP, then the condition

$$\begin{aligned} l_i(q^*) \mu_i^* = 0, \quad 1 \leq i \leq z \\ \mu_i^* > 0, \quad i \in \mathcal{I}_{ac} \end{aligned} \quad (10)$$

Is called strict complementary slackness at q^* . Matrix L is described with the derivate of active constraints as follows:

$$L(q) = (\nabla k_1(q), \dots, \nabla k_m(q), \nabla l_{i_1}(q), \dots, \nabla l_{i_j}(q)) \quad (11)$$

where ∇ represents the gradient operator and j represents the number of active constraints. For $f(q^*)$ that is a local minimum of the NLP assumed existing of λ^* and μ^* such that

$$\begin{aligned} \nabla \mathcal{L}(q^*, \lambda^*, \mu^*) = \nabla f(q^*) + \nabla k(q^*) \lambda^* \\ + \nabla l(q^*) \mu^* = 0 \end{aligned} \quad (12)$$

If equation (17) carries true, hence the condition is known as the first-order necessary optimality condition. Suppose the following criteria are encountered:

- 1) The columns of $L(q^*)$ are linearly independent,
- 2) Strict complementarity slackness holds at q^* ,

3) The Hessian of the Lagrangian with respect to q is positive definite on the null space of $L(q^*)^T$,

Thereafter, equation (6) and these prerequisites are referred to as the second-order enough optimality conditions of the NLP, and the Lagrangian multipliers λ and μ^* are distinctively defined.

After describing the constraints that must be fulfilled in order to take some value as a minimum, the QP for each iteration step is requisite to be constructed. The QP sub-problems represent the NLP's local properties with regard to the existing iteration $p[k]$. As a result, the objective function f is substituted with its local quadratic probability distribution:

$$f(p) \approx f(q[p]) + \nabla f(q[p])(q - q[p]) + \frac{1}{2}(q - q[p])Kf(q[p])(q - q[p]) \quad (13)$$

and constraint functions l and k are replaced with their local affine approximations:

$$l(q) \approx l(q[p]) + \nabla l(q[p])(q - q[p]) \quad (14)$$

$$k(q) \approx k(q[p]) + \nabla k(q[p])(q - q[p]) \quad (15)$$

where $\nabla f(q)$ represents the gradient of function and $Kf(q)$ Hessian of function. For optimization purposes, we assign the bounds parameter between 0 and 1. As shown in Fig. 2, in the initial iteration, it takes the total number of Snapshots T , and we reiterate the T to the total number of 25 times (O_1, \dots, O_N) to acquire the local optimum and generate the best ensemble selection.

G. Activation Function

Activation functions have been a main field of research in order to fully understand the training complexity of neural networks. Whereas activation functions have played a significant part, in practical application paradigms, they have been regarded as a sole element, whereas in theoretical areas such as Mean Field Theory (MFT), they have been regarded as a primary component, the discussion over activation functions is becoming more volatile. Whereas ReLU and Leaky ReLU have transformed the area due to their ease of formulation and low computational complexity, several studies have presented smoother versions to enhance optimization and information propagation like ELU, Softplus, and Swish [96]. However, they have largely been one-hit adventures, failing to adopt versatile data sets. In this paper in order to tackle the versatile spatial-spectral feature datasets, we propose a novel activation function called Relish. The graphical implementation of Relish activation function has been shown in Fig.3. The details of the equation of the proposed activation function are given below. To recap, Relish is defined as:

$$Y = X * \max(0, \beta x) \quad (16)$$

$$f(x) = \begin{cases} 0, & \text{if } x < 0 \\ x, & \text{if } x \geq 0 \end{cases} \quad (17)$$

where $f(x) = \max(0, x)$ is the Relu activation function and β is either a constant or a trainable parameter. Fig. 3 shows the graph of Relish for the value of $\beta = 0.1$. As seen in Fig. 3, it has a few key subtly different characteristics that distinguish it from other activation functions. Firstly, Relish is a smooth continuous function like Swish. Since Relish threshold values all negative weights to zero whereas Swish enables a few negative weights to pass through. This Relish characteristic is critical to the effectiveness of non-monotonic smooth activation functions when employ in our Deep Hyperspectral Shots method to classify spatial-spectral features. Finally, the trainable parameter ensures finer tuning of the activation function in order to boost spatial-spectral feature propagation and advance for smoother gradients, this tends to make the landscape simpler to optimize, allowing for smoother and faster generalization of the proposed method. The complete algorithmic description of our proposed Deep Hyperspectral Shots is expressed in algorithm 2.

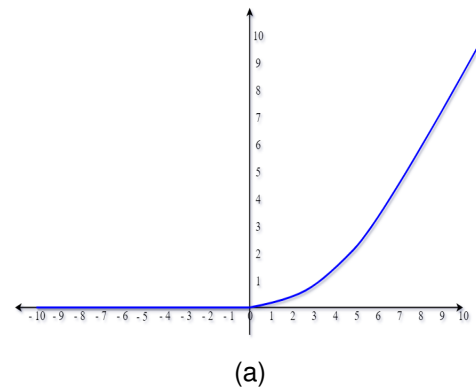


Fig. 3 Shows the plot of the proposed Relish activation function.

III. EXPERIMENT AND RESULT ANALYSIS

In this section, the comprehensive description of three different HSI data sets acquired by using various imaging technologies that include Indian Pines (IP), University of Pavia (PU), and Salinas (SA)¹, the experimental configuration is first thoroughly stated. Then, the hyper-parameters setting of the method, the results, the discussion, and the comparison between the proposed and the state-of-the-art methods are investigated and discussed. Furthermore, the experimental depiction of the different hyper-parameter and analyses are illustrated and evaluated.

A. Data Description

In this section, we employed three various types of widely employed data sets to investigate the effectiveness of our proposed method. The source images and ground truths of three various hyperspectral datasets are illustrated in Fig. 4, Fig. 5, and Fig. 6.

- 1) 1) The first dataset SA was captured by the AVIRIS sensor through the geographical area of Salinas Valley,

¹<http://lesun.weebly.com/hyperspectral-data-set.html>

Algorithm 2 Deep Hyperspectral Shots

Require: \mathbf{Z} : Hyperspectral images data; \mathbf{N} : total number of classes; \mathbf{M} : total number of training samples; \mathbf{L} : Snapshot; **SCB**: Snapshot Callback; **epc**: epoch per cycle; n_epoch : total number of epochs of each cycle; \mathbf{T} : total number of Snapshots; \mathbf{V} : number of Snapshots Required; y_v : prediction of Snapshots; $E = \phi$: an ensemble.

- 1: **Procedure**
- 2: Apply FA to execute the dimensionality reduction process for \mathbf{N} of HSI datasets \mathbf{Z}
- 3: Obtain the training samples \mathbf{M} by arbitrary selection \mathbf{N} pixels from the spectral-spatial dataset \mathbf{Z} , generate the testing samples \mathbf{MT} by the remaining pixels
- 4: Retrieve the spatial features from the hyperspectral images datasets \mathbf{Z} and acquire the spectral-spatial fusion information by using the wavelet transform method.
- 5: **Training Phase:**
- 6: **for** CallBack = **SCB** **do:**
- 7: initialize \mathbf{L}
- 8: Execute above Equation (4), and (5)
- 9: After each iteration n_epoch save learning rate
- 10: **if** $epoch \neq 0$ & $(epoch+1) \% epc == 0$: **do:**
- 11: Generate and Save trained \mathbf{L} model.
- 12: **end if**
- 13: **if** $\mathbf{T} = \mathbf{V}$:
- 14: Execute \mathbf{T} to optimize
- 15: **end if**
- 16: **Testing Phase:**
- 17: Generate prediction y_v by feeding the testing \mathbf{MT} into the trained \mathbf{T} model and E
- 18: **end for**

Ensure:

- 19: Ensemble \mathbf{T} : $E = T_1, T_2, \dots, T_n$
- 20: Final prediction: $y^* = \arg \max \sum_{t=1}^T 1(y_v = g), g = 1, 2, \dots, g$

CA, USA, with a spatial resolution of 3.7 m/pixel. The Salinas scene is made up of 224 spectral bands composed of the wavelength range of 360 to 2500nm and 512×217 pixels as shown in Table I. The data set includes 16 classes made concerning vegetables, vineyard fields, and bare soil. Table II depicts the number of classes and includes training and test data of this data set.

- 2) The second dataset PU was collected by an unmanned aerial optical device the Reflective Optics Spectrographic Imaging System over Pavia, Italy, in 2002. (ROSIS). The aircraft was managed by the German Aerospace Center as part of the HySens venture, which was funded by the European Union. After discarding 12 noisy channels, the data set mainly comprises 640×340 pixels with a 1.3 m/pixel spatial resolution and 103 bands containing the wavelength range of 430 to 860 nm as shown in Table I. Moreover, the whole dataset is comprised of nine classes. The comprehensive details of different classes are given in Table III.
- 3) The third dataset is the Purdue Indiana Indian Pines

TABLE I
DETAILED DESCRIPTION OF EACH DATASET USED DURING EXPERIMENT

Name	Spatial Dimension	Spectral Bands	Wavelength Range	Classes
SA	512x217	224	360nm - 2500nm	16
UP	610x340	103	430nm - 860nm	9
IP	145x145	224	400nm - 2500nm	16

TABLE II
AMOUNTS OF TRAINING AND TEST DATA OF THE SALINAS DATASET

Class No.	Class Name	Training	Test
1	Brocoli_green_weeds_1	201	1808
2	Brocoli_green_weeds_2	373	3353
3	Fallow	198	1778
4	Fallow_rough_plow	140	1254
5	Fallow_smooth	268	2410
6	Stubble	396	3563
7	Celery	358	3221
8	Grapes_untrained	1128	10143
9	Soil_vinyard_develop	621	5582
10	Corn_senesced_green_weeds	328	2950
11	Lettuce_romaine_4wk	107	961
12	Lettuce_romaine_5wk	193	1734
13	Lettuce_romaine_6wk	92	824
14	Lettuce_romaine_7wk	107	963
15	Vinyard_untrained	727	6,541
16	Vinyard_vertical_trellis	181	1626
	Total	5418	48711

scene IP, which was acquired from the Indian Pines testing site in North-Western Indiana. The data resolution is 145×145 , and it incorporates 200 spectral bands. It covers 145×145 pixels with a 20-m/pixel spatial resolution and 224 spectral bands comprised from 400 to 2500 nm. The ground truth appends 16 classes of interest, which are largely diverse crops in various growth stages as given in Table I, and IV.

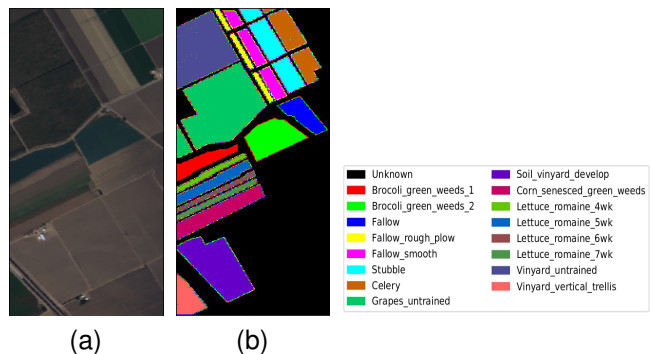


Fig. 4 Shows the SA dataset. (a) source image, and (b) ground truth.

TABLE III
AMOUNTS OF TRAINING AND TEST DATA OF THE PAVIA UNIVERSITY DATASET

Class No.	Class Name	Training	Test
1	Asphalt	664	5967
2	Medows	1865	16784
3	Gravel	210	1889
4	Tress	307	2757
5	Painted Metal sheets	135	1210
6	Self-Blocking Bare soil	503	4526
7	Bitumen	133	1197
8	Bricks	369	3313
9	Shadows	664	5967
Total		4850	43610

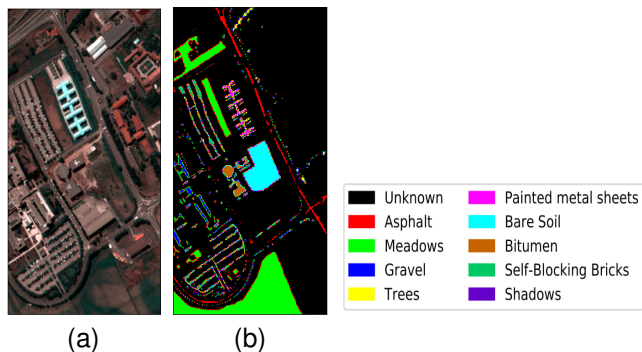


Fig. 5 Shows the PU dataset. (a) source image, and (b) ground truth.

TABLE IV
AMOUNTS OF TRAINING AND TEST DATA OF THE INDIAN PINES SCENE DATASET

Class No.	Class Name	Training	Test
1	Alfalfa	5	41
2	Corn-notill	143	1285
3	Corn-mintill	83	747
4	Corn	24	213
5	Grass-pasture	49	434
6	Grass-trees	73	657
7	Grass-pasture-mowed	3	25
8	Hay-windrowed	48	430
9	Oats	2	18
10	Soybean-notill	98	874
11	Soybean-mintill	246	2209
12	Soybean-clean	60	533
13	Wheat	21	184
14	Woods	127	1138
15	Buildings-grass-trees	39	347
16	Stone-steel-towers	10	83
Total		1031	9218

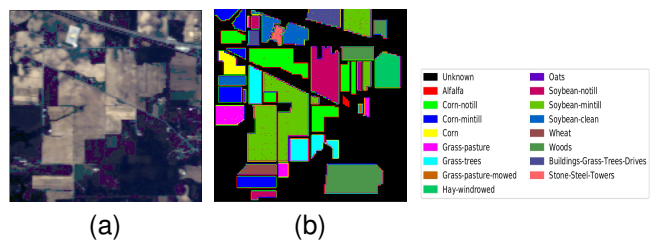


Fig. 6 Shows the IP dataset. (a) source image, and (b) ground truth.

B. Experimental Configuration

To investigate the efficiencies of the proposed HSIC model, a number of the-state-of-the-art methods were compared with DHS, including SVM-RBF², CCF-200³, 2D CNN [44], GCNN [70], FADCNN [97], NL-GCNN [98], DWR-DEL [99], E-CNN-PPF-SSF [100]. Moreover, we also compare the proposed Activation function with other techniques on the three data sets. We set the total number of epochs to 500, number of depths of CNN and Wavelet and Wavelet decomposition is considered 4, the learning rate of Activation Function is set to 0.1, the number of components of FA is set to 75, and the standard test ratio is considered 0.9, with the window size 24. The total number of ensemble size is set to 10 and n cycles per epoch is fixed at 50.

The following evaluation metrics are used to quantitatively compare various methods for hyperspectral data classification computations from various perspectives. Detailed information on each evaluation metric is given below.

- 1) **Overall Accuracy (OA):** To evaluate the performance of HSIC methods the first standard evaluation metric is OA. The metric is calculated as the fraction of test samples that are differentiated correctly.
- 2) **Average Accuracy (AA):** In order to assess the performance of the method with respect to each class in the dataset, we compute per-class accuracy performance with respect to each category in a data set, and we also compute per-class accuracy. This metric is calculated as the average of all per-class accuracies.
- 3) **Kappa Coefficient (K):** The most common evaluation metric used in the HSIC is K, this statistical evaluation metric is an aspect of the declaration of validity standard measure.

C. Performance Comparison of Methods

- 1) **SVM-RBF:** A SVM method with the extensively utilized Radial Basis Function (RBF) kernel. We employ five-fold cross-validation to find the optimum hyper-parameters and C (maintaining the sensitivity of penalization throughout model optimization) in the range of $y = 2^{-3}, 2^{-2}, \dots, 2^4$ and $C = 10^{-2}, 10^{-1}, \dots, 10^4$.
- 2) **CCF-200:** This technique is a traditional spectral-spatial HSIC method that, for the first time, employs EPF to design feature representations of HSIs.

²<https://www.csie.ntu.edu.tw/~cjlin/libsvm/>

³<https://github.com/twgr/ccfs>

- 3) **2D CNN:** This method used iterative feedback to initiate HSIC, capturing and integrating spatial contextual information to enhance classification accuracy. The spectral signature of the particular class analyzed with the label, employed in the Gaussian filter, is set to 0.5 with a window size of 5, and the stopping threshold is 0.99 in this method.
- 4) **GCNN:** It generated a sparse feature map for HSI data incorporating numerous features extracted using various spatial-based filters. In order to implement the replica, we use four types of features with a sparsity level of three in our method.
- 5) **FADCNN:** The bi-directional RNN is constructed by training in both positive and negative time directions at the same time. Instead of using spectrum data as a training instance, we used spatial patches with a size of 13×13 in the experiment. In our deployment, there are three hidden layers, each with 60 nodes. The other set contains a batch size of 20, 5000 iterations, and a $1e-4$ learning rate.
- 6) **NL-GCNN:** This method consists of a baseline 34-layer ResNets for HSIC. The applied settings of each residual block are used with the following hyper-parameters, set the total number of epochs to 5000, and the learning rate of $1e-4$.
- 7) **DWR-DEL:** This method consists of two dynamic ensemble learning techniques using local weighted residual (LWR-DEL) and double-weighted residual (DWR-DEL) for HSIC. The range of regularization parameters λ in the classification models are fixed as (1e-2, 1e-4, 1e-6). The framework consist of 15 core classification models.
- 8) **E-CNN-PPF-SSF:** This method used a deep ensemble CNN based on sample expansion for HSIC. In order to implement the method, we set the total number of epochs to 900 and the learning rate decays every 300 epochs with a decay rate of 0.01 and the ensemble total size is set to 5.
- 9) **DHS:** This is our proposed method, the proposed method is a multi-snapshot ensemble feedforward neural network that consists of five explicit functional parts, such as the Pre-processing part, the base or core model, Snapshots Generation, Snapshot Optimization and Ensemble Selection, and finally the Output part. The details of hyperparameters are given in section B.

We employ OA, AA, and K as objective measures to analyze the effectiveness of all the comparison methodologies in the subsequent experiments. Each network implementation has been reiterated five times, and the OA calculation has been described. All of the approaches were built on the TensorFlow framework, with the running environment consisting of an NVidia P100 Tesla with 16 Gb, and 128 GB RAM. The batch size is set to 1024, and the proposed networks are trained for 500 Epochs with a 0.1 learning rate. The cyclic annealing algorithm is chosen as an optimizer, with the HSI data dropout rate set to 0.4, and the training sample size is 64×64 . Furthermore, Tables II, III, and IV mentioned the total number of training and testing sets samples for the three

HSI datasets.

The first experiment is being carried out on the Salinas dataset. After the FA block, the data size is converted to $64 \times 64 \times 3$ and the training ratio is assigned to 10% similarly to the previous two datasets. The ground truth and predicted classification maps are shown in Fig. 7, and classification results based on OAs metric are depicted in Table V. We can observe that OAs produced by our proposed method are higher with a score of 99.96% comparably with the state-of-the-art methods E-CNN-PPF-SSF with a score of 99.18%, DWR-DEL with a score of 93.27%, NL-GCNN with a score of 92.28%, FADCNN a score of 90.58%, GCNN with a score of 90.37%, and also against the conventional methods 2D-CNN, CCF-200 and SVM-RBF with a score of 90.25%, 82.87%, and, 74.24% respectively.

Similarly, the proposed DHS shows higher AA scores with 99.97% against the state-of-the-art and traditional methods with scores of 99.58%, 96.82%, 92.28%, 97.80%, 97.80%, 85.43%, 85.43%, 90.25%, 82.87%, and 74.24% respectively as illustrated in the Table V. Moreover, we also compared the results of our proposed method DHS based K, as we can see, DHS has a comparatively robust and well-balanced classification impact for each class and produce the highest scores, and outperformed the state-of-the-art and traditional methods with scores of 99.95%.

In the second experiment Purdue Indiana Indian Pines scene, 10% of the training samples were randomly chosen, and the input data dimensions after FA is $64 \times 64 \times 3$. The classification result is based on IP dataset of AA, OA, and K, a comparison with the state-of-the-art methods is shown in Table. IV. The ground truth, and predicted maps are illustrated in Fig. 8. As demonstrated in Table. IV, the DHS obtained the highest OA of 97.91%. It can be observed that the proposed model has a significant impact on the HSI dataset performance. Furthermore, we can observe that DHS outperforms E-CNN-PPF-SSF at 97.91%, DWR-DEL at 89.13%, NL-GCNN at 87.92%, FADCNN at 97.80%, and GCNN at 85.43% indicating that the DHS approach is useful and necessary for the HSIC.

Based on AA Evaluation metric the proposed DHS 97.14% method also performed well against the state-of-the-art methods with lower scores of E-CNN-PPF-SSF 97.14%, DWR-DEL 93.81%, NL-GCNN 93.79%, FADCNN 93.96%, and GCNN 91.87%, it shows that DHS can effectively classify the HIC dataset. The experimental results of all methods have been shown in the Table VI.

The final experiment is being carried out on the PU dataset to validate the performance of our proposed method. The training sample percentage of the PU is set to 10%, we kept the sample size of the PU dataset after FA similar to IP $64 \times 64 \times 3$. Fig. 9 shows the ground truth and predicted classification maps of the proposed method and other methods.

As illustrated in Table VII, it can be observed that the DHS method acquired the leading OA of 99.49%, which is higher than E-CNN-PPF-SSF at 99.10%, DWR-DEL at 98.41%, NL-GCNN at 90.04%, GCNN at 87.08%, and slightly higher than FADCNN at 99.19%. In contrast, the other methods only produce lower scores of OA. The main factor is that the PU data set has a comparatively sparse feature density, so the

TABLE V
CLASSIFICATION ACCURACIES OF PROPOSED DEEP HYPERSPECTRAL SHOTS IN TERMS OF OA, KAPPA, AND AA AGAINST THE STATE-OF-THE-ART METHODS SALINAS DATA SET

No.	Class Names	SVM-RBF	CCF-200	2D CNN	GCNN	FADCNN	NL-GCNN	DWR-DEL	E-CNN-PPF-SSF	DHS
1	Brocoli_green_weeds_1	98.98	99.49	71.57	99.59	88.26	99.69	99.61	100	100
2	Brocoli_green_weeds_2	99.67	99.95	99.86	98.07	98.04	99.21	99.45	100	100
3	Fallow	98.70	99.43	88.89	91.95	98.04	99.79	99.59	100	100
4	Fallow_rough_plow	97.77	99.33	98.14	97.84	97.13	98.29	99.01	100	100
5	Fallow_smooth	98.33	98.82	98.17	98.06	99.13	99.28	99.35	100	99.97
6	Stubble	99.72	99.80	100	99.00	99.10	99.80	99.21	100	100
7	Celery	99.46	99.66	97.00	99.29	99.21	99.04	99.23	100	99.97
8	Grapes_untrained	70.37	67.56	70.79	82.25	75.72	79.11	84.12	98.21	99.98
9	Soil_vinyard_develop	98.59	99.19	99.45	97.11	100	97.74	97.10	100	100
10	Corn_senesced_green_weeds	93.74	93.80	96.19	91.60	79.00	95.01	94.91	99.33	99.93
11	Lettuce_romaine_4wk	94.70	95.87	96.37	90.77	95.3	94.60	96.01	100	100
12	Lettuce_romaine_5wk	99.89	99.95	100	100	98.34	100	100	100	100
13	Lettuce_romaine_6wk	97.81	98.15	100	98.96	95.12	98.96	98.67	100	100
14	Lettuce_romaine_7wk	97.35	96.86	98.33	97.35	98.86	99.41	99.54	99.37	100
15	Vinyard_untrained	71.53	80.77	91.22	70.44	99.23	84.26	85.11	97.23	99.80
16	Vinyard_vertical_trellis	98.18	98.18	93.00	97.10	83.53	98.01	98.21	100	100
OA	-	88.82	89.72	90.25	90.37	90.58	92.28	93.27	99.18	99.96
AA	-	94.67	95.43	93.69	94.34	94.56	96.39	96.82	99.58	99.97
K	-	87.57	88.58	89.18	89.28	90.25	89.64	91.97	98.17	99.95

TABLE VI
CLASSIFICATION ACCURACIES OF PROPOSED DEEP HYPERSPECTRAL SHOTS IN TERMS OF OA, KAPPA, AND AA AGAINST THE STATE-OF-THE-ART METHODS THE INDIAN PINES SCENE DATA SET

No.	Class Names	SVM-RBF	CCF-200	2D CNN	GCNN	FADCNN	NL-GCNN	DWR-DEL	E-CNN-PPF-SSF	DHS
1	Alfalfa	71.39	76.37	54.77	76.66	88.26	83.09	95.45	91.35	98.01
2	Corn-notill	71.05	77.93	96.94	86.10	98.04	89.03	72.19	95.50	95.50
3	Corn-mintill	86.96	94.57	99.46	100	97.04	100	84.45	97.51	95.02
4	Corn	91.72	94.41	96.87	93.06	96.03	93.51	81.41	97.32	97.32
5	Grass-pasture	85.80	91.39	94.12	92.06	99.34	94.12	88.29	98.10	98.10
6	Grass-trees	93.85	97.04	96.81	96.81	99.48	98.18	99.42	99.53	99.53
7	Grass-pasture-mowed	75.38	90.96	91.29	88.24	75.72	88.24	100	100	100
8	Hay-windrowed	59.88	69.48	93.05	76.80	100	78.78	100	100	100
9	Oats	76.24	89.01	87.59	80.85	78.00	86.70	100	92.30	92.30
10	Soybean-notill	96.91	98.77	100	99.38	96.50	99.38	86.80	96.12	96.12
11	Soybean-mintill	79.58	93.73	68.57	93.89	98.49	94.94	92.46	98.64	98.64
12	Soybean-clean	74.84	74.55	88.48	93.64	95.45	97.27	79.46	94.56	94.56
13	Wheat	97.78	100	100	100	99.02	100	100	100	100
14	Woods	79.49	97.44	82.05	92.31	99.48	97.44	99.43	99.78	99.78
15	Buildings-Grass-Trees-Drives	100	90.91	100	100	99.74	100	94.81	98.70	98.70
16	Stone-Steel-Towers	100	100	100	100	82.80	100	93.22	90.60	90.60
OA	-	74.24	82.87	90.25	85.43	97.80	87.92	89.13	97.91	97.91
AA	-	83.80	89.78	93.69	91.87	93.96	93.79	93.81	97.14	97.14
K	-	70.93	80.59	89.18	83.42	86.10	86.25	88.18	96.26	96.26

TABLE VII
CLASSIFICATION ACCURACIES OF PROPOSED DEEP HYPERSPECTRAL SHOTS IN TERMS OF OA, KAPPA, AND AA AGAINST THE STATE-OF-THE-ART METHODS THE PAVIA UNIVERSITY DATA SET

No.	Class Names	SVM-RBF	CCF-200	2D CNN	GCNN	FADCNN	NL-GCNN	DWR-DEL	E-CNN-PPF-SSF	DHS
1	Asphalt	82.37	86.59	83.85	78.89	99.70	86.80	97.69	99.08	99.57
2	Meadows	67.87	72.33	96.09	90.50	99.75	88.74	98.01	100	100
3	Gravel	69.18	71.75	81.47	71.70	94.31	70.84	98.33	94.45	98.43
4	Trees	98.37	99.09	96.12	98.76	99.10	98.43	99.07	99.09	99.50
5	Painted metal sheets	99.41	99.78	98.74	99.93	99.82	99.85	100	100	100
6	Bare Soil	93.64	97.26	49.79	79.08	99.92	94.37	99.52	100	100
7	Bitumen	91.20	91.88	79.32	71.20	96.97	86.24	100	99.09	98.41
8	Self-Blocking Bricks	92.59	94.92	88.89	92.83	97.90	96.74	98.05	96.15	99.78
9	Shadows	96.94	98.73	94.19	97.47	98.97	95.78	100	99.95	98.53
OA	-	78.89	83.36	86.93	87.08	99.19	90.04	98.41	99.10	99.49
AA	-	87.95	90.26	85.38	86.71	98.49	90.87	98.99	98.41	99.36
K	-	74.91	79.05	82.42	83.07	95.25	87.06	98.04	95.37	99.31

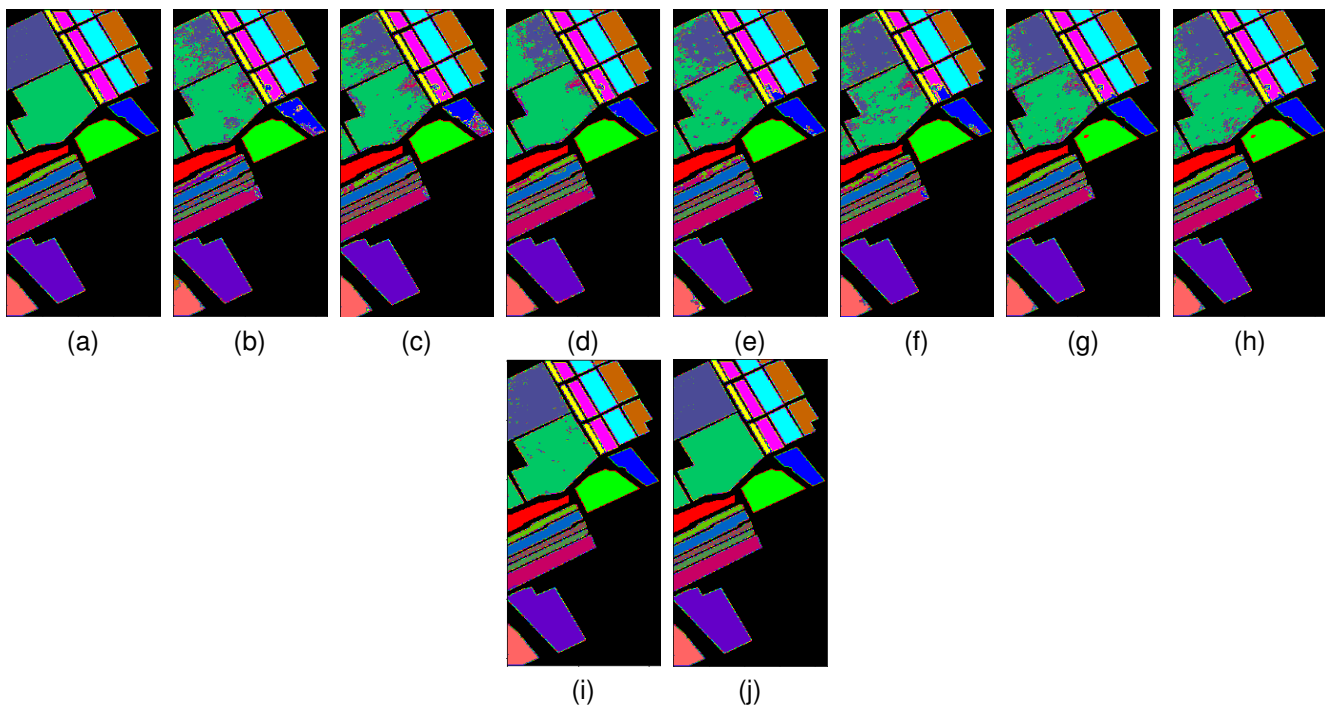


Fig. 7 Shows the classification maps of various methods for the Salinas data set. (From Left to Right) (a) groundtruth, (b) SVM-RBF, (c) CCF-200, (d) 2-D CNN, (e) GCNN , (f) FADCNN, (g) NL-GCNN, (h) DWR-DEL, (i) E-CNN-PPF-SSF and (j) DHS.

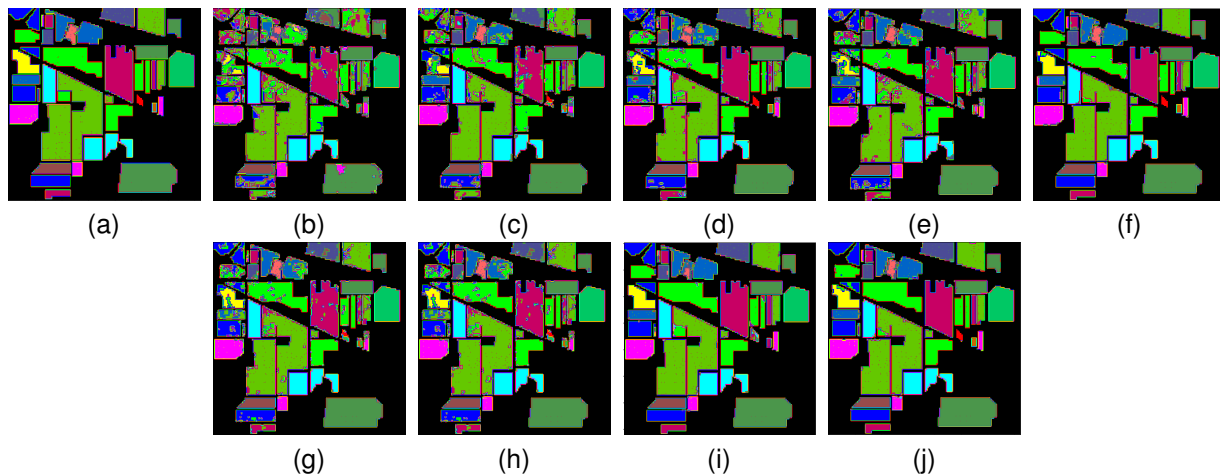


Fig. 8 Shows the classification maps of various methods for the Indian Pines data set. (From Left to Right and from top to bottom) (a) groundtruth, (b) SVM-RBF, (c) CCF-200, (d) 2-D CNN, (e) GCNN , (f) FADCNN, (g) NL-GCNN, (h) DWR-DEL, (i) E-CNN-PPF-SSF and (j) DHS.

conventional methods have more complexity in representing the spectral-spatial feature. While with the DHS with Snapshot and Relish execution, the proposed method acquired higher accuracy compared to the other state-of-the-art methods, which validates the proposed DHS has the capabilities with the enhanced feature description. Furthermore, the Principal Component Analysis based proposed methods performed the low, with OA indicating that the representation of the primary components has a troubling impact on the dense feature extraction for the HSI data with the feature of high sparsity. In comparison, our method with the FA, Snapshot ensemble, and Relish activation function

module have better sparsity durability. We also performed experiments based on AA and K accuracy metrics, as Table. VII shows that our proposed method outperformed the state-of-the-art methods with scores of 99.36%, and 99.31% respectively. The DHS method demonstrates the high performance and high reliability of HSIC in all of the experiments performed on the three data sets.

IV. DISCUSSION

To thoroughly validate the effectiveness of our proposed method, we perform a number of experiments, incorporating

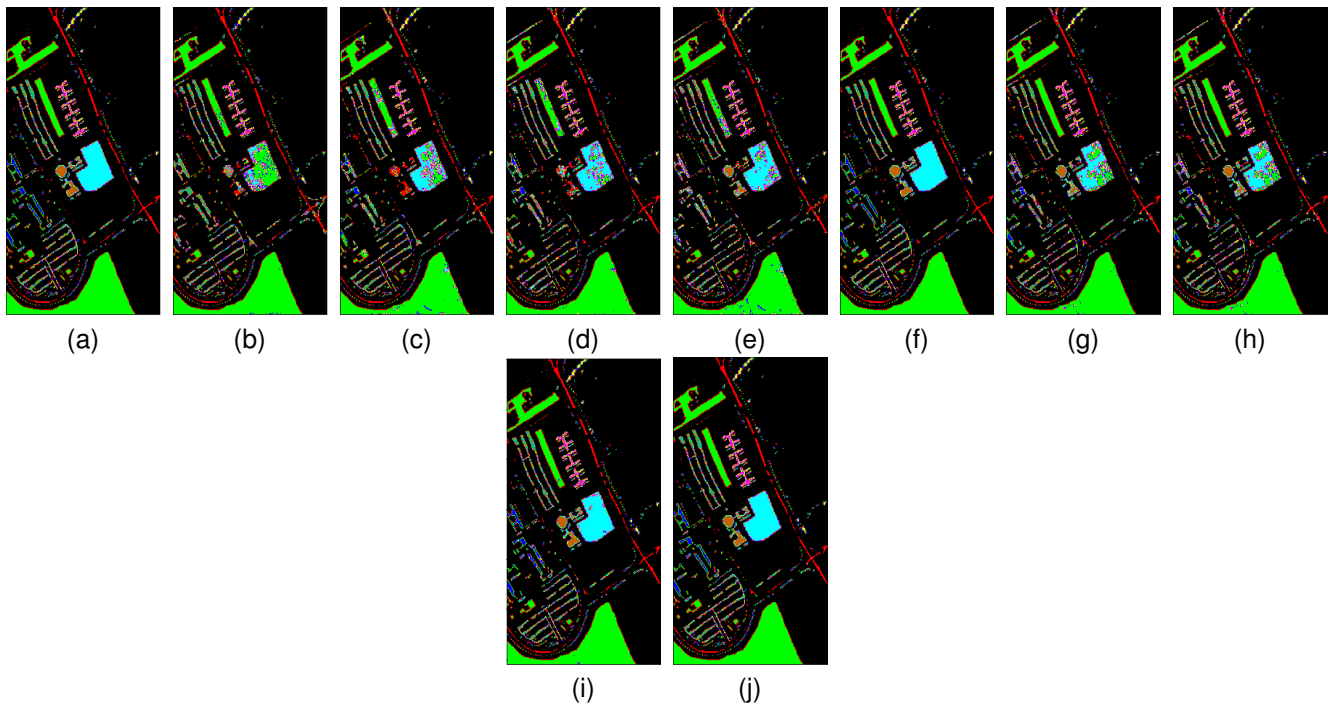


Fig. 9 Shows the classification maps of various methods for the Pavia University data set. (From Left to Right) (a) ground truth, (b) SVM-RBF, (c) CCF-200, (d) 2-D CNN, (e) GCNN , (f) FADCNN, (g) NL-GCNN, (h) DWR-DEL, (i) E-CNN-PPF-SSF and (j) DHS.

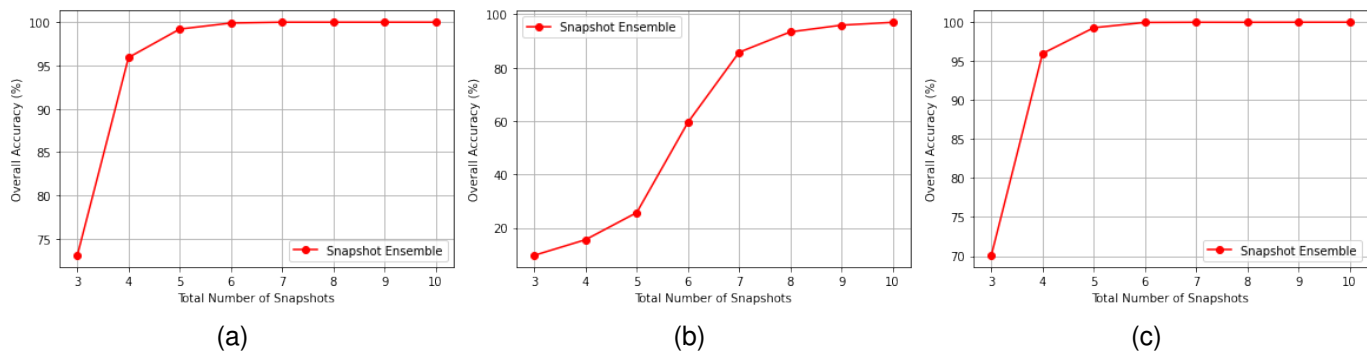


Fig. 10 Shows the OA effect of Snapshots Ensemble of the proposed method on data sets of (a) SA, (b) IP, and (c) PU.

the effect of each part and scalability.

A. Analysis of the Effect of Snapshots Ensemble

Fig. 10 demonstrates the effectiveness of DHS with various numbers of Snapshot models ensemble On three datasets. The Snapshot models are chosen from the DHS intermediary models trained after every 50 iterations. As the results show, the efficiency variability is not very substantial when the range of snapshot models is increased from 6 to 8, indicating that DHS can reach fair accuracy also without optimized snapshot model preference.

Furthermore, in this experiment, choosing 1-10 snapshot models can obtain relatively improved results than others. This suggests that utilizing numerous snapshot models, e.g., 15, could reduce prediction performance if several low-performance models may be chosen. This inference is aligned with findings

from other ensemble learning research findings, in which researchers discovered that if the efficiency of the core models is too terrible, the ensemble efficiency may suffer [101], [102]. However, thanks to the strong ensemble selection Even so, because of DHS robust ensemble sampling adaptability, the ensemble efficiency does not deteriorate significantly even when we choose 10 snapshot models. As we can see in Fig.10, a, b, and c the Performance of the DHS is consistently increasing on SA, and PU datasets after 1 to 4 with the increasing number of snapshots, while the performance on the IP dataset increased after 5 to 6. Hence, this demonstrates that our proposed DHS method is effective for HSIC datasets.

B. Analysis of the Depth of Snapshots

The depth of the base models is very important for any ensemble-based method. In order to optimize the efficiency of

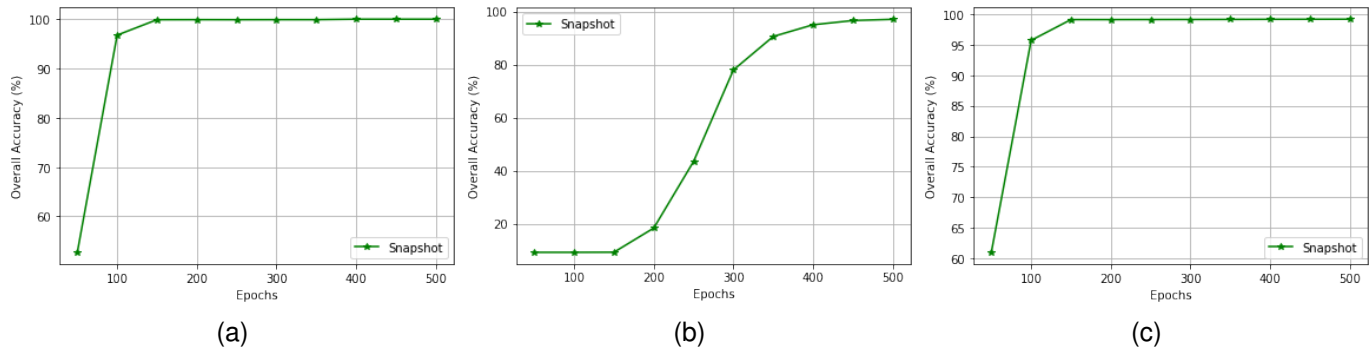


Fig. 11 Shows the OA Depth of Snapshots results based on data sets of (a) SA, (b) IP, and (c) PU.

our proposed DHS, we performed a number of experiments to validate the efficiency. In Fig. 11, we can see that the performance of the model was lower at the beginning, but the performance increased with an increasing number of the depth of Snapshots.

In this paper, we select the total number of Snapshots depth of only 10 and left the remaining sizes for future work. The performance of Snapshot at depth of 3 is 99.88% OA on dataset SA, 99.03% OA with dataset PU dataset, and 9.53% OA with dataset IP, when the number of Snapshot depth increased to 7 the performance of the model increased to 99.89% OA on SA dataset and 99.12% OA on PU dataset, and also on 90.74% OA on IP dataset. Moreover, when we kept the final Snapshot depth the 10 the performance of the method increases to 99.89% OA on SA dataset, 99.13% OA on PU dataset, and finally 97.20% OA on IP dataset. Hence, it shows that the depth of Snapshots has a significant role to enhance the performance of the method in terms of overall accuracy.

C. Analysis of Depth of Model

Numerous latest findings have illustrated that DNNs can substantially enhance the efficacy of a wide range of artificial intelligence applications, including CV, and NLP. ResNeXt [103] is the most recent promising DNN for CV issues, and it has demonstrated outstanding results.

A ResNeXt model has been built upon a total of 50, 101 layers in order to acquire top performance. In our proposed method, we use a DNN tower structure to allow the model to learn additional spatial-spectral features of three different dataset information. We utilize DHS with 28 CNN layers within the framework of the tower formation, and each layer has 256, 128, and 64, respectively with the concatenation of wavelet transform levels. If the network topology map is designed by 64 neurons with the first layer, it can be expressed as (64). Same as if the depth of the DHS second part of layers with 128, it can be expressed as $\langle 128, 64 \rangle$. Similarly, the third part of the CNN layer with 256 (256, 128, 64) and the fourth part of the CNN layers also with same layers of parameters of 256 (256, 256, 128, 64) respectively. As a result, if the depth of the CNN layers is I, thereafter the DHS Topological architecture is as described in the following: $[24^{2i1}, 23^{2i2}, \dots, 24]$.

Fig. 12 shows the confusion matrix of various depths of a model that when the total number of CNN layers is increased from 4, 5, and 6, efficiency slowly increases, indicating that the depth of a Deep Neural Network can increase the model's efficiency. Moreover, in IP dataset the proposed model performed poorly with the increasing number of CNN and wavelet transforms, the core reason of that the total number of the training sample size of IP dataset is very less. Furthermore, we also increased the Wavelet Transform decomposition layers number, which increase the sparsity of the IP dataset leading to the performance of IP dataset in decline. Although the performance on remaining datasets boosts the performance of DHS additionally, DNN capabilities must not be underestimated.

D. Analysis of Hyperparameter Effect

In this section, the effects of three various parameters on the DHS model's efficiency are investigated: 0.1, 0.01, and 0.001. Because of the vital spatial feature engaged, the learning rate of the deep learning training sample is critical for improving HSIC accuracy. In general, the small-scale learning rate relatively increased efficiency. Consequently, a lower learning rate of the training sample eventually results in the train-test data overlapping. On the one hand, we suppose that the size specification is appropriate for exploiting the plentiful local feature. On the other hand, we believe that this specification is not substantial to cause overlapping problems.

According to the comprehensive experimental findings, Fig. 13 (a), (b), and (c) shows qualitative analyses of classification results with identical training sample size for all three different data sets. Particularly, the OA initially enhance with a learning rate of 0.001 and decreases for the Indian Pines dataset. As we can see, when the learning rate of the proposed method changed to 0.01, the performance gets enhanced with an improved accuracy score of 95.96% on IP dataset, 99.21% on Pu dataset, and an accuracy of 99.95% score on Salinas dataset. Specifically, the OA gets the highest value, when we integrate a 0.01 learning rate in our method the performance significantly improved on three datasets. The OA accuracy rates are mainly steadily improving, with a more influential learning rate of 0.1, and the classification accuracy achieves its pinnacle. As we can observe in Fig.13, the OA obtains the highest score for the

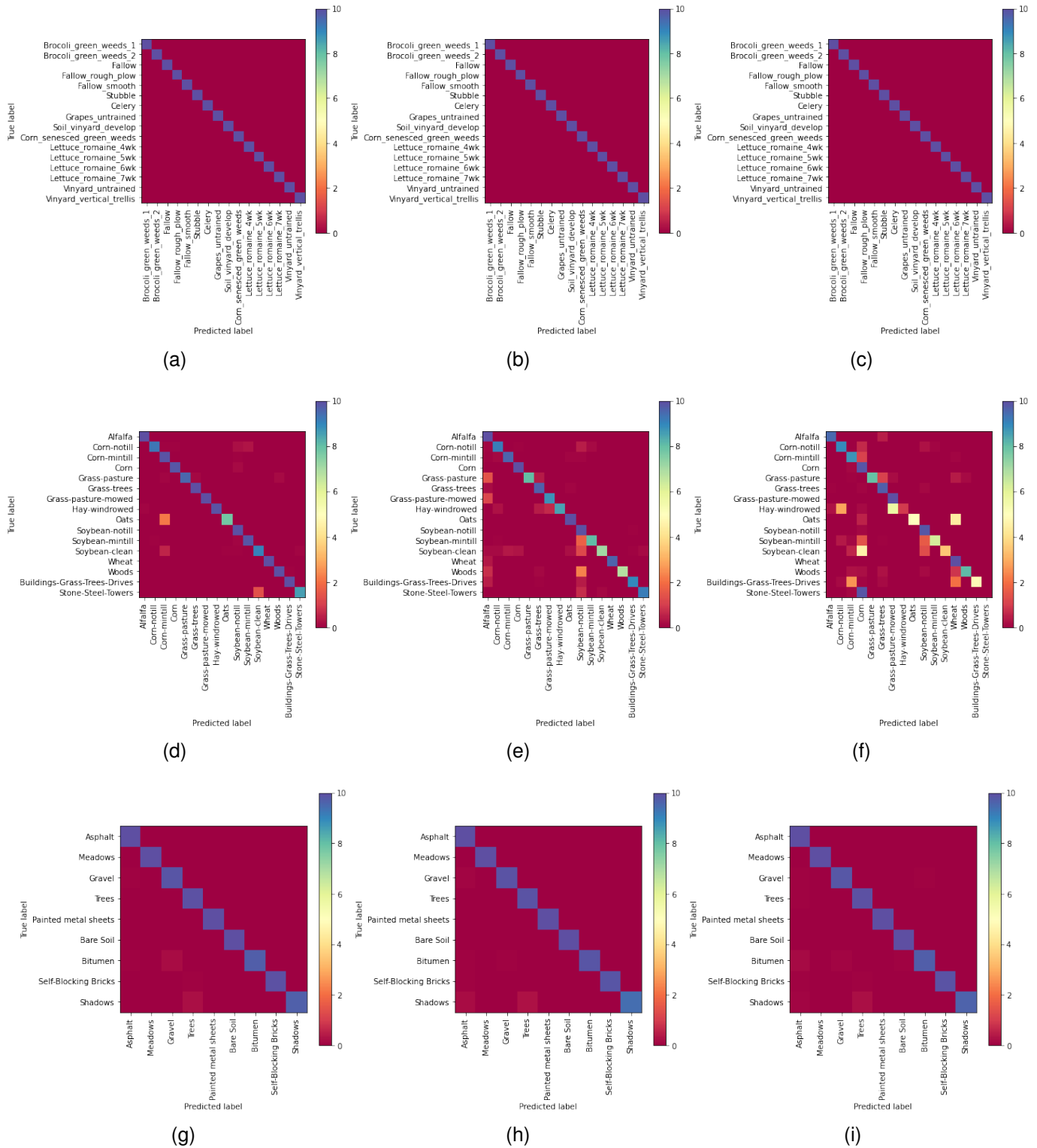


Fig. 12 Shows the confusion matrix of the impact of the depth of the proposed method on data sets of (a)-(c) SA, (d)-(f) IP, and (g)-(i) PU.

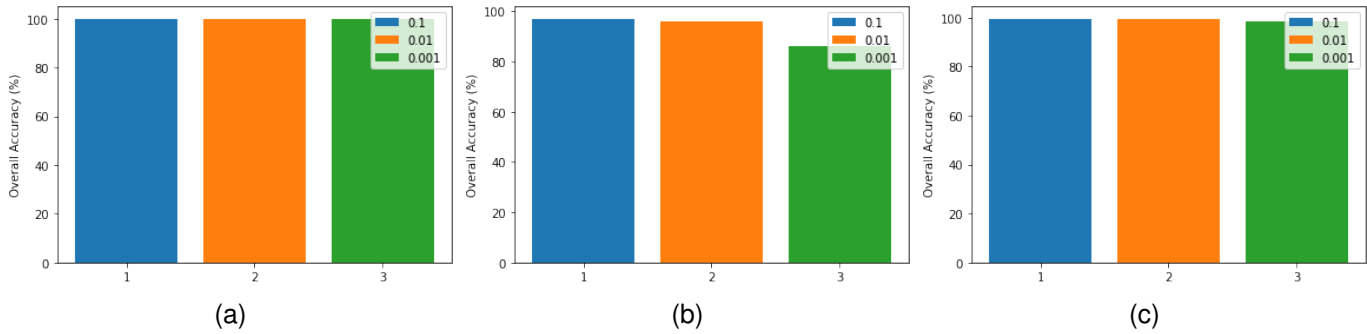


Fig. 13 Shows the impact of different hyperparameter effects on the proposed method on data sets of (a) SA (b) IP, and (c) PU.

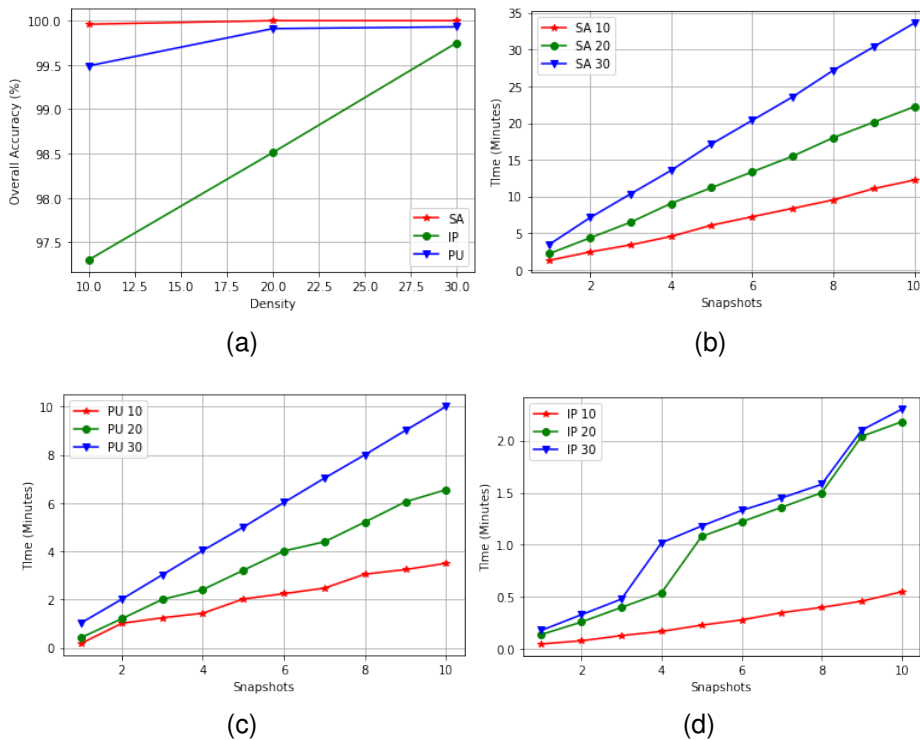


Fig. 14 Shows the Scalability results of the proposed method on three hyperspectral datasets. (a) Shows the Response time of the proposed method of SA, PU, and IP datasets, (b) shows the Throughput on SA dataset, (c) shows the Throughput on PU dataset, and (d) shows the Throughput on IP dataset.

Salinas dataset 99.96%. When the learning rate is set to 0.1, our method generates the best accuracy of 99.49% achieved with the Purdue University dataset respectively. Moreover, the accuracy score for the Indian Pines dataset is also improved with an accuracy score of 97.91%. Comparatively, it demonstrates that the larger the learning rate in our proposed method with spatial information implied is beneficial for improving accuracy.

E. Scalability

We evaluated the scalability of our proposed method by employing two criteria: Response Time and Throughput. We run experimental studies on the SA, PU, and IP datasets at three various densities of 10%, 20%, and 30% training samples. Fig. 14 (a), (b), (c), and (d) show that the proposed method

performed well on a density of 10% at SA data set, with scores of 99.96% OA, and Time of 12 minutes and 25 seconds. The score of the density of 10% on PU data set is 99.49% OA with a total time of 3 minutes and 50 seconds. Similarly, the score on IP data set is 97.91% OA with a total time of 55 seconds. We also conduct experiments on the 20% density of three data sets. The performance score of 20% on SA data set is 100% OA with a total time of 22 minutes and 21 seconds. The performance score of PU dataset also acquired the 99.91% OA with a total time of 6 minutes and 55 seconds. The performance score of IP is 98.51% OA with a total time of 2 minutes and 18 seconds. Furthermore, we also evaluated experiments on 30% density on three data sets. The OA accuracy value of SA data set is 100% with a total time of 33 minutes and 58

seconds. The OA score on PU is also 99.93% with a total time of 10 minutes and 2 seconds. Lastly, the IP data set to acquire 99.75% OA with a total time of 2 minutes and 25 seconds. In particular, the scalability of Machine Learning (ML) techniques relates to a collection of ML and deep learning models that can handle various amounts of data and parameters. This highly variable number of datasets can either be building the model, which is known as the training step, or after the model has been built, which is known as the testing or execution step. When the model is developed, scalability corresponds to the model's ability to perform well across a range of test datasets and hyperparameters. The effectiveness of the deep learning approach is also highly subjective and depends on a variety of hyper-parameters. For instance, performance can be improved through optimization of memory consumption or improved recognition performance regardless of the testing data sizes and characteristics. Furthermore, the best scalable deep learning techniques should generalize effectively and enable for computational efficiency of large datasets.

In terms of the Deep Hyperspectral Snapshots and the above interpretations of scalability, our method is very effective. Because the method is constructed with training and testing-based validation, hence, the efficiency noted is the outcome of a significant percentage of iterations that mainly portray a realistic real-world scenario. In terms of ensemble integration, Deep Hyperspectral Snapshots enable a very scalable method of deep learning where the number of new models is integrated by just training a single core model. This not only minimizes computation iterations but moreover improves OA results. Deep learning generates numerous real-time applications for scalability in the massive dataset. Deep learning has been shown to be effective in a wide range of practical and real-world issues when it comes to testing new and diverse datasets. As a result, we believe our method takes benefit of the latest advances in deep learning techniques, resulting in a plausible, effective, and scalable approach. Based on the experimental results in Fig.14, we observed that the proposed method presents a scalable approach.

V. CONCLUSION

In this article, we propose a novel Deep Hyperspectral Shots, a deep smooth wavelet convolutional neural network shots ensemble for hyperspectral image classification. A deep smooth wavelet CNN incorporates the layers of wavelet transform to extract spectral features. Furthermore, computing a wavelet transform is computationally lighter than 3D CNN. After spectral features extraction, it is concatenated to the 2D CNN which extracts the spatial features, thus establishing a spatial-spectral feature vector for classification. Furthermore, we present the Snapshots generation method and employ Cyclic Annealing schedule (CAS) to converge to various local minimums along its optimization path and save the base model. We build several snapshots of the Deep Hyperspectral Shots model to enhance performance. We introduce the snapshots optimization and ensemble selection approach in order to solve the optimization problem within ensemble creation and further enhance the performance. Furthermore, we also present a novel

Relish activation function that has been integrated into the proposed method to boost spatial-spectral feature propagation and advance for smoother gradients. Experimental results and analysis show that our proposed method DHS achieved overall accuracies (OAs) of 99.96%, 97.91%, and 99.49% on the Salinas, Indian Pines and Pavia University datasets against the state-of-the-art methods.

In future work, we will improve the proposed method by integrating the latest approaches, thereby expanding its suitability for HSI classification tasks. Additionally, we will build a lightweight ensemble that maintains classification performance while lessening computational complexity. Moreover, we will explore how incorporating state-of-the-art Vision Transformers models into our proposed method can enhance the interpretability of HSI data features. Alongside this, there is potential for extending the application of DHS method to various tasks like semantic segmentation and object detection, opening new avenues for research.

REFERENCES

- [1] X. Jia, B.-C. Kuo, and M. M. Crawford, "Feature mining for hyperspectral image classification," *Proceedings of the IEEE*, vol. 101, no. 3, pp. 676–697, 2013.
- [2] P. Ghamisi, N. Yokoya, J. Li, W. Liao, S. Liu, J. Plaza, B. Rasti, and A. Plaza, "Advances in hyperspectral image and signal processing: A comprehensive overview of the state of the art," *IEEE Geoscience and Remote Sensing Magazine*, vol. 5, no. 4, pp. 37–78, 2017.
- [3] S. Roessner, K. Segl, U. Heiden, and H. Kaufmann, "Automated differentiation of urban surfaces based on airborne hyperspectral imagery," *IEEE Transactions on Geoscience and Remote Sensing*, vol. 39, no. 7, pp. 1525–1532, 2001.
- [4] G. Camps-Valls, D. Tuia, L. Bruzzone, and J. A. Benediktsson, "Advances in hyperspectral image classification: Earth monitoring with statistical learning methods," *IEEE signal processing magazine*, vol. 31, no. 1, pp. 45–54, 2013.
- [5] J. Li, I. Dópido, P. Gamba, and A. Plaza, "Complementarity of discriminative classifiers and spectral unmixing techniques for the interpretation of hyperspectral images," *IEEE Transactions on Geoscience and Remote Sensing*, vol. 53, no. 5, pp. 2899–2912, 2014.
- [6] F. F. Sabins, "Remote sensing for mineral exploration," *Ore geology reviews*, vol. 14, no. 3-4, pp. 157–183, 1999.
- [7] F. Melgani and L. Bruzzone, "Classification of hyperspectral remote sensing images with support vector machines," *IEEE Transactions on geoscience and remote sensing*, vol. 42, no. 8, pp. 1778–1790, 2004.
- [8] B. Waske, S. van der Linden, J. A. Benediktsson, A. Rabe, and P. Hostert, "Sensitivity of support vector machines to random feature selection in classification of hyperspectral data," *IEEE Transactions on Geoscience and Remote Sensing*, vol. 48, no. 7, pp. 2880–2889, 2010.
- [9] L. Ma, M. M. Crawford, and J. Tian, "Local manifold learning-based k -nearest-neighbor for hyperspectral image classification," *IEEE Transactions on Geoscience and Remote Sensing*, vol. 48, no. 11, pp. 4099–4109, 2010.
- [10] Y. Zhang, G. Cao, X. Li, and B. Wang, "Cascaded random forest for hyperspectral image classification," *IEEE journal of selected topics in applied earth observations and remote sensing*, vol. 11, no. 4, pp. 1082–1094, 2018.
- [11] M. Khodadadzadeh, J. Li, A. Plaza, and J. M. Bioucas-Dias, "A subspace-based multinomial logistic regression for hyperspectral image classification," *IEEE Geoscience and Remote Sensing Letters*, vol. 11, no. 12, pp. 2105–2109, 2014.
- [12] W. Li, C. Chen, H. Su, and Q. Du, "Local binary patterns and extreme learning machine for hyperspectral imagery classification," *IEEE Transactions on Geoscience and Remote Sensing*, vol. 53, no. 7, pp. 3681–3693, 2015.
- [13] Y. Tarabalka, M. Fauvel, J. Chanussot, and J. A. Benediktsson, "Svm-and mrf-based method for accurate classification of hyperspectral images," *IEEE Geoscience and Remote Sensing Letters*, vol. 7, no. 4, pp. 736–740, 2010.

- [14] X. Kang, S. Li, and J. A. Benediktsson, "Spectral-spatial hyperspectral image classification with edge-preserving filtering," *IEEE transactions on geoscience and remote sensing*, vol. 52, no. 5, pp. 2666–2677, 2013.
- [15] M. Fauvel, J. A. Benediktsson, J. Chanussot, and J. R. Sveinsson, "Spectral and spatial classification of hyperspectral data using svms and morphological profiles," *IEEE Transactions on Geoscience and Remote Sensing*, vol. 46, no. 11, pp. 3804–3814, 2008.
- [16] P. Quesada-Barruiuso, F. Argüello, and D. B. Heras, "Spectral-spatial classification of hyperspectral images using wavelets and extended morphological profiles," *IEEE Journal of Selected Topics in Applied Earth Observations and Remote Sensing*, vol. 7, no. 4, pp. 1177–1185, 2014.
- [17] B. Hou, T. Huang, and L. Jiao, "Spectral-spatial classification of hyperspectral data using 3-d morphological profile," *IEEE Geoscience and Remote Sensing Letters*, vol. 12, no. 12, pp. 2364–2368, 2015.
- [18] L. Fang, S. Li, X. Kang, and J. A. Benediktsson, "Spectral-spatial hyperspectral image classification via multiscale adaptive sparse representation," *IEEE Transactions on Geoscience and Remote sensing*, vol. 52, no. 12, pp. 7738–7749, 2014.
- [19] J. Liu, Z. Wu, Z. Wei, L. Xiao, and L. Sun, "Spatial-spectral kernel sparse representation for hyperspectral image classification," *IEEE Journal of Selected Topics in Applied Earth Observations and Remote Sensing*, vol. 6, no. 6, pp. 2462–2471, 2013.
- [20] L. He, J. Li, A. Plaza, and Y. Li, "Discriminative low-rank gabor filtering for spectral-spatial hyperspectral image classification," *IEEE Transactions on Geoscience and Remote Sensing*, vol. 55, no. 3, pp. 1381–1395, 2016.
- [21] C. J. Della Porta, A. A. Bekit, B. H. Lampe, and C.-I. Chang, "Hyperspectral image classification via compressive sensing," *IEEE Transactions on Geoscience and Remote Sensing*, vol. 57, no. 10, pp. 8290–8303, 2019.
- [22] Q. Wang, Z. Meng, and X. Li, "Locality adaptive discriminant analysis for spectral-spatial classification of hyperspectral images," *IEEE Geoscience and Remote Sensing Letters*, vol. 14, no. 11, pp. 2077–2081, 2017.
- [23] H. Yuan, Y. Y. Tang, Y. Lu, L. Yang, and H. Luo, "Spectral-spatial classification of hyperspectral image based on discriminant analysis," *IEEE Journal of Selected Topics in Applied Earth Observations and Remote Sensing*, vol. 7, no. 6, pp. 2035–2043, 2013.
- [24] D. L. Donoho *et al.*, "High-dimensional data analysis: The curses and blessings of dimensionality," *AMS math challenges lecture*, vol. 1, no. 2000, p. 32, 2000.
- [25] A. Krizhevsky, I. Sutskever, and G. E. Hinton, "Imagenet classification with deep convolutional neural networks," *Advances in neural information processing systems*, vol. 25, 2012.
- [26] C. Szegedy, W. Liu, Y. Jia, P. Sermanet, S. Reed, D. Anguelov, D. Erhan, V. Vanhoucke, and A. Rabinovich, "Going deeper with convolutions," in *Proceedings of the IEEE conference on computer vision and pattern recognition*, 2015, pp. 1–9.
- [27] F. Ullah, B. Zhang, and R. U. Khan, "Image-based service recommendation system: A jpeg-coefficient rfs approach," *IEEE Access*, vol. 8, pp. 3308–3318, 2020.
- [28] J. Long, E. Shelhamer, and T. Darrell, "Fully convolutional networks for semantic segmentation," in *Proceedings of the IEEE conference on computer vision and pattern recognition*, 2015, pp. 3431–3440.
- [29] R. Girshick, "Fast r-cnn," in *Proceedings of the IEEE international conference on computer vision*, 2015, pp. 1440–1448.
- [30] A. Bordes, X. Glorot, J. Weston, and Y. Bengio, "Joint learning of words and meaning representations for open-text semantic parsing," in *Artificial intelligence and statistics*. PMLR, 2012, pp. 127–135.
- [31] F. Ullah, B. Zhang, R. U. Khan, T.-S. Chung, M. Attique, K. Khan, S. E. Khediri, and S. Jan, "Deep edu: A deep neural collaborative filtering for educational services recommendation," *IEEE Access*, vol. 8, pp. 110915–110928, 2020.
- [32] E. Merényi, W. H. Farrand, J. V. Taranik, and T. B. Minor, "Classification of hyperspectral imagery with neural networks: comparison to conventional tools," *EURASIP Journal on Advances in Signal Processing*, vol. 2014, no. 1, pp. 1–19, 2014.
- [33] L. Mou, P. Ghamisi, and X. X. Zhu, "Deep recurrent neural networks for hyperspectral image classification," *IEEE Transactions on Geoscience and Remote Sensing*, vol. 55, no. 7, pp. 3639–3655, 2017.
- [34] R. Hang, Q. Liu, D. Hong, and P. Ghamisi, "Cascaded recurrent neural networks for hyperspectral image classification," *IEEE Transactions on Geoscience and Remote Sensing*, vol. 57, no. 8, pp. 5384–5394, 2019.
- [35] Y. Xu, L. Zhang, B. Du, and F. Zhang, "Spectral-spatial unified networks for hyperspectral image classification," *IEEE Transactions on Geoscience and Remote Sensing*, vol. 56, no. 10, pp. 5893–5909, 2018.
- [36] F. Zhou, R. Hang, Q. Liu, and X. Yuan, "Hyperspectral image classification using spectral-spatial lstms," *Neurocomputing*, vol. 328, pp. 39–47, 2019.
- [37] Y. Chen, Z. Lin, X. Zhao, G. Wang, and Y. Gu, "Deep learning-based classification of hyperspectral data," *IEEE Journal of Selected topics in applied earth observations and remote sensing*, vol. 7, no. 6, pp. 2094–2107, 2014.
- [38] P. Zhong, Z. Gong, S. Li, and C.-B. Schönlieb, "Learning to diversify deep belief networks for hyperspectral image classification," *IEEE Transactions on Geoscience and Remote Sensing*, vol. 55, no. 6, pp. 3516–3530, 2017.
- [39] Y. Chen, X. Zhao, and X. Jia, "Spectral-spatial classification of hyperspectral data based on deep belief network," *IEEE Journal of Selected Topics in Applied Earth Observations and Remote Sensing*, vol. 8, no. 6, pp. 2381–2392, 2015.
- [40] J. Yang, Y.-Q. Zhao, and J. C.-W. Chan, "Learning and transferring deep joint spectral-spatial features for hyperspectral classification," *IEEE Transactions on Geoscience and Remote Sensing*, vol. 55, no. 8, pp. 4729–4742, 2017.
- [41] N. Li and Z. Wang, "Hyperspectral image ship detection based upon two-channel convolutional neural network and transfer learning," in *2020 IEEE 5th International Conference on Signal and Image Processing (ICSIP)*. IEEE, 2020, pp. 88–92.
- [42] Y. Chen, H. Jiang, C. Li, X. Jia, and P. Ghamisi, "Deep feature extraction and classification of hyperspectral images based on convolutional neural networks," *IEEE Transactions on Geoscience and Remote Sensing*, vol. 54, no. 10, pp. 6232–6251, 2016.
- [43] C. Wang, N. Ma, Y. Ming, Q. Wang, and J. Xia, "Classification of hyperspectral imagery with a 3d convolutional neural network and jm distance," *Advances in space research*, vol. 64, no. 4, pp. 886–899, 2019.
- [44] Z. Ge, G. Cao, X. Li, and P. Fu, "Hyperspectral image classification method based on 2d-3d cnn and multibranch feature fusion," *IEEE Journal of Selected Topics in Applied Earth Observations and Remote Sensing*, vol. 13, pp. 5776–5788, 2020.
- [45] J. Zheng, Y. Feng, C. Bai, and J. Zhang, "Hyperspectral image classification using mixed convolutions and covariance pooling," *IEEE Transactions on Geoscience and Remote Sensing*, vol. 59, no. 1, pp. 522–534, 2020.
- [46] K. He, X. Zhang, S. Ren, and J. Sun, "Deep residual learning for image recognition," in *Proceedings of the IEEE conference on computer vision and pattern recognition*, 2016, pp. 770–778.
- [47] Z. Zhong, J. Li, Z. Luo, and M. Chapman, "Spectral-spatial residual network for hyperspectral image classification: A 3-d deep learning framework," *IEEE Transactions on Geoscience and Remote Sensing*, vol. 56, no. 2, pp. 847–858, 2017.
- [48] M. E. Paoletti, J. M. Haut, R. Fernandez-Beltran, J. Plaza, A. J. Plaza, and F. Pla, "Deep pyramidal residual networks for spectral-spatial hyperspectral image classification," *IEEE Transactions on Geoscience and Remote Sensing*, vol. 57, no. 2, pp. 740–754, 2018.
- [49] X. Zhang, Y. Wang, N. Zhang, D. Xu, H. Luo, B. Chen, and G. Ben, "Spectral-spatial fractal residual convolutional neural network with data balance augmentation for hyperspectral classification," *IEEE Transactions on Geoscience and Remote Sensing*, vol. 59, no. 12, pp. 10473–10487, 2021.
- [50] Y. Xu, Z. Li, W. Li, Q. Du, C. Liu, Z. Fang, and L. Zhai, "Dual-channel residual network for hyperspectral image classification with noisy labels," *IEEE Transactions on Geoscience and Remote Sensing*, vol. 60, pp. 1–11, 2021.
- [51] J. M. Haut, M. E. Paoletti, J. Plaza, A. Plaza, and J. Li, "Visual attention-driven hyperspectral image classification," *IEEE transactions on geoscience and remote sensing*, vol. 57, no. 10, pp. 8065–8080, 2019.
- [52] J. Su, J. Zeng, D. Xiong, Y. Liu, M. Wang, and J. Xie, "A hierarchy-to-sequence attentional neural machine translation model," *IEEE/ACM Transactions on Audio, Speech, and Language Processing*, vol. 26, no. 3, pp. 623–632, 2018.
- [53] F. Wang, M. Jiang, C. Qian, S. Yang, C. Li, H. Zhang, X. Wang, and X. Tang, "Residual attention network for image classification," in *Proceedings of the IEEE conference on computer vision and pattern recognition*, 2017, pp. 3156–3164.
- [54] S. Woo, J. Park, J.-Y. Lee, and I. S. Kweon, "Cbam: Convolutional block attention module," in *Proceedings of the European conference on computer vision (ECCV)*, 2018, pp. 3–19.
- [55] L. Mou and X. X. Zhu, "Learning to pay attention on spectral domain: A spectral attention module-based convolutional network for hyperspectral

- image classification," *IEEE Transactions on Geoscience and Remote Sensing*, vol. 58, no. 1, pp. 110–122, 2019.
- [56] L. Zhao, J. Yi, X. Li, W. Hu, J. Wu, and G. Zhang, "Compact band weighting module based on attention-driven for hyperspectral image classification," *IEEE Transactions on Geoscience and Remote Sensing*, vol. 59, no. 11, pp. 9540–9552, 2021.
- [57] P. Shamsolmoali, M. Zareapoor, J. Chanussot, H. Zhou, and J. Yang, "Rotation equivariant feature image pyramid network for object detection in optical remote sensing imagery," *IEEE Transactions on Geoscience and Remote Sensing*, vol. 60, pp. 1–14, 2022.
- [58] M. Zhu, L. Jiao, F. Liu, S. Yang, and J. Wang, "Residual spectral-spatial attention network for hyperspectral image classification," *IEEE Transactions on Geoscience and Remote Sensing*, vol. 59, no. 1, pp. 449–462, 2020.
- [59] Z. Lu, B. Xu, L. Sun, T. Zhan, and S. Tang, "3-d channel and spatial attention based multiscale spatial-spectral residual network for hyperspectral image classification," *IEEE Journal of Selected Topics in Applied Earth Observations and Remote Sensing*, vol. 13, pp. 4311–4324, 2020.
- [60] W. Ma, Q. Yang, Y. Wu, W. Zhao, and X. Zhang, "Double-branch multi-attention mechanism network for hyperspectral image classification," *Remote Sensing*, vol. 11, no. 11, p. 1307, 2019.
- [61] L. Li, J. Yin, X. Jia, S. Li, and B. Han, "Joint spatial-spectral attention network for hyperspectral image classification," *IEEE geoscience and remote sensing letters*, vol. 18, no. 10, pp. 1816–1820, 2020.
- [62] N. Li and Z. Wang, "Spectral-spatial fused attention network for hyperspectral image classification," in *2021 IEEE International Conference on Image Processing (ICIP)*. IEEE, 2021, pp. 3832–3836.
- [63] H. Sun, X. Zheng, X. Lu, and S. Wu, "Spectral-spatial attention network for hyperspectral image classification," *IEEE Transactions on Geoscience and Remote Sensing*, vol. 58, no. 5, pp. 3232–3245, 2019.
- [64] Z. Zhao, D. Hu, H. Wang, and X. Yu, "Center attention network for hyperspectral image classification," *IEEE Journal of Selected Topics in Applied Earth Observations and Remote Sensing*, vol. 14, pp. 3415–3425, 2021.
- [65] Z. Zhong, Y. Li, L. Ma, J. Li, and W.-S. Zheng, "Spectral-spatial transformer network for hyperspectral image classification: A factorized architecture search framework," *IEEE Transactions on Geoscience and Remote Sensing*, vol. 60, pp. 1–15, 2021.
- [66] J. He, L. Zhao, H. Yang, M. Zhang, and W. Li, "Hsi-bert: Hyperspectral image classification using the bidirectional encoder representation from transformers," *IEEE Transactions on Geoscience and Remote Sensing*, vol. 58, no. 1, pp. 165–178, 2019.
- [67] X. He and Y. Chen, "Optimized input for cnn-based hyperspectral image classification using spatial transformer network," *IEEE Geoscience and Remote Sensing Letters*, vol. 16, no. 12, pp. 1884–1888, 2019.
- [68] H. Yan, J. Wang, L. Tang, E. Zhang, K. Yan, K. Yu, and J. Peng, "A 3d cascaded spectral-spatial element attention network for hyperspectral image classification," *Remote Sensing*, vol. 13, no. 13, p. 2451, 2021.
- [69] R. Li, S. Zheng, C. Duan, Y. Yang, and X. Wang, "Classification of hyperspectral image based on double-branch dual-attention mechanism network," *Remote Sensing*, vol. 12, no. 3, p. 582, 2020.
- [70] D. Hong, L. Gao, J. Yao, B. Zhang, A. Plaza, and J. Chanussot, "Graph convolutional networks for hyperspectral image classification," *IEEE Transactions on Geoscience and Remote Sensing*, vol. 59, no. 7, pp. 5966–5978, 2020.
- [71] W. Liao, M. Dalla Mura, J. Chanussot, and A. Pižurica, "Fusion of spectral and spatial information for classification of hyperspectral remote-sensed imagery by local graph," *IEEE Journal of Selected Topics in Applied Earth Observations and Remote Sensing*, vol. 9, no. 2, pp. 583–594, 2015.
- [72] H. Huang, G. Shi, H. He, Y. Duan, and F. Luo, "Dimensionality reduction of hyperspectral imagery based on spatial-spectral manifold learning," *IEEE transactions on cybernetics*, vol. 50, no. 6, pp. 2604–2616, 2019.
- [73] H. Huang, Y. Duan, H. He, and G. Shi, "Local linear spatial-spectral probabilistic distribution for hyperspectral image classification," *IEEE Transactions on Geoscience and Remote Sensing*, vol. 58, no. 2, pp. 1259–1272, 2019.
- [74] Z. Feng, S. Yang, M. Wang, and L. Jiao, "Learning dual geometric low-rank structure for semisupervised hyperspectral image classification," *IEEE Transactions on Cybernetics*, vol. 51, no. 1, pp. 346–358, 2019.
- [75] Z. Zhang, Y. Ding, X. Zhao, L. Siye, N. Yang, Y. Cai, and Y. Zhan, "Multireceptive field: An adaptive path aggregation graph neural framework for hyperspectral image classification," *Expert Systems with Applications*, vol. 217, p. 119508, 2023.
- [76] Y. Ding, Z. Zhang, X. Zhao, D. Hong, W. Cai, N. Yang, and B. Wang, "Multi-scale receptive fields: Graph attention neural network for hyperspectral image classification," *Expert Systems with Applications*, vol. 223, p. 119858, 2023.
- [77] Y. Ding, Z. Zhang, X. Zhao, D. Hong, W. Li, W. Cai, and Y. Zhan, "Af2gnn: Graph convolution with adaptive filters and aggregator fusion for hyperspectral image classification," *Information Sciences*, vol. 602, pp. 201–219, 2022.
- [78] Z. Chen, G. Wu, H. Gao, Y. Ding, D. Hong, and B. Zhang, "Local aggregation and global attention network for hyperspectral image classification with spectral-induced aligned superpixel segmentation," *Expert Systems with Applications*, p. 120828, 2023.
- [79] F. Luo, B. Du, L. Zhang, L. Zhang, and D. Tao, "Feature learning using spatial-spectral hypergraph discriminant analysis for hyperspectral image," *IEEE transactions on cybernetics*, vol. 49, no. 7, pp. 2406–2419, 2018.
- [80] Y. Zhou, J. Peng, and C. P. Chen, "Dimension reduction using spatial and spectral regularized local discriminant embedding for hyperspectral image classification," *IEEE Transactions on Geoscience and Remote Sensing*, vol. 53, no. 2, pp. 1082–1095, 2014.
- [81] Z. Feng, S. Yang, S. Wang, and L. Jiao, "Discriminative spectral-spatial margin-based semisupervised dimensionality reduction of hyperspectral data," *IEEE Geoscience and Remote Sensing Letters*, vol. 12, no. 2, pp. 224–228, 2014.
- [82] E. Zhang, X. Zhang, L. Jiao, L. Li, and B. Hou, "Spectral-spatial hyper-spectral image ensemble classification via joint sparse representation," *Pattern Recognition*, vol. 59, pp. 42–54, 2016.
- [83] Y. Zhang, G. Cao, A. Shafique, and P. Fu, "Label propagation ensemble for hyperspectral image classification," *IEEE Journal of Selected Topics in Applied Earth Observations and Remote Sensing*, vol. 12, no. 9, pp. 3623–3636, 2019.
- [84] F. Gao, Q. Wang, J. Dong, and Q. Xu, "Spectral and spatial classification of hyperspectral images based on random multi-graphs," *Remote Sensing*, vol. 10, no. 8, 2018.
- [85] N. Laban, B. Abdellatif, H. M. Ebeid, H. A. Shedeed, and M. F. Tolba, "Reduced 3-d deep learning framework for hyperspectral image classification," in *International Conference on Advanced Machine Learning Technologies and Applications*. Springer, 2019, pp. 13–22.
- [86] S. Fujieda, K. Takayama, and T. Hachisuka, "Wavelet convolutional neural networks," *arXiv preprint arXiv:1805.08620*, 2018.
- [87] —, "Wavelet convolutional neural networks for texture classification," *arXiv preprint arXiv:1707.07394*, 2017.
- [88] X. Wang, "Moving window-based double haar wavelet transform for image processing," *IEEE Transactions on image processing*, vol. 15, no. 9, pp. 2771–2779, 2006.
- [89] P. Liu, H. Zhang, K. Zhang, L. Lin, and W. Zuo, "Multi-level wavelet-cnn for image restoration," in *Proceedings of the IEEE conference on computer vision and pattern recognition workshops*, 2018, pp. 773–782.
- [90] K. He, X. Zhang, S. Ren, and J. Sun, "Deep residual learning for image recognition," in *Proceedings of the IEEE conference on computer vision and pattern recognition*, 2016, pp. 770–778.
- [91] G. Huang, Z. Liu, L. Van Der Maaten, and K. Q. Weinberger, "Densely connected convolutional networks," in *Proceedings of the IEEE conference on computer vision and pattern recognition*, 2017, pp. 4700–4708.
- [92] L. N. Smith, "No more pesky learning rate guessing games," *CoRR*, *abs/1506.01186*, vol. 5, p. 363, 2015.
- [93] N. Tong, H. Lu, X. Ruan, and M.-H. Yang, "Salient object detection via bootstrap learning," in *Proceedings of the IEEE Conference on Computer Vision and Pattern Recognition (CVPR)*, June 2015.
- [94] M. Yang, J. Crenshaw, B. Augustine, R. Mareachen, and Y. Wu, "Adaboost-based face detection for embedded systems," *Computer Vision and Image Understanding*, vol. 114, no. 11, pp. 1116–1125, 2010.
- [95] C. Zhang, J. Yan, C. Li, and R. Bie, "Contour detection via stacking random forest learning," *Neurocomputing*, vol. 275, pp. 2702–2715, 2018.
- [96] P. Ramachandran, B. Zoph, and Q. V. Le, "Searching for activation functions," *arXiv preprint arXiv:1710.05941*, 2017.
- [97] C. Yu, R. Han, M. Song, C. Liu, and C.-I. Chang, "Feedback attention-based dense cnn for hyperspectral image classification," *IEEE Transactions on Geoscience and Remote Sensing*, vol. 60, pp. 1–16, 2021.
- [98] L. Mou, X. Lu, X. Li, and X. X. Zhu, "Nonlocal graph convolutional networks for hyperspectral image classification," *IEEE Transactions on Geoscience and Remote Sensing*, vol. 58, no. 12, pp. 8246–8257, 2020.

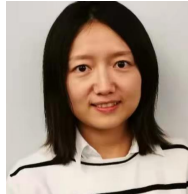
- [99] H. Lu, H. Su, P. Zheng, Y. Gao, and Q. Du, "Weighted residual dynamic ensemble learning for hyperspectral image classification," *IEEE Journal of Selected Topics in Applied Earth Observations and Remote Sensing*, vol. 15, pp. 6912–6927, 2022.
- [100] S. Dong, W. Feng, Y. Quan, G. Dauphin, L. Gao, and M. Xing, "Deep ensemble cnn method based on sample expansion for hyperspectral image classification," *IEEE Transactions on Geoscience and Remote Sensing*, vol. 60, pp. 1–15, 2022.
- [101] Z.-H. Zhou, J. Wu, and W. Tang, "Ensembling neural networks: many could be better than all," *Artificial intelligence*, vol. 137, no. 1-2, pp. 239–263, 2002.
- [102] A. Krogh and J. Vedelsby, "Neural network ensembles, cross validation, and active learning," *Advances in neural information processing systems*, vol. 7, 1994.
- [103] S. Xie, R. Girshick, P. Dollár, Z. Tu, and K. He, "Aggregated residual transformations for deep neural networks," in *Proceedings of the IEEE conference on computer vision and pattern recognition*, 2017, pp. 1492–1500.



computer vision.

Farhan Ullah received the B.Sc. and M.C.S. degrees in computer science from the University of Peshawar and Sarhad University of Science and Information Technology, Peshawar, Pakistan, in 2013 and 2015, respectively, and the Ph.D. degree from the Shanghai University, Shanghai, China, in 2020.

Currently, he is working as a Post-Doctoral fellow with the College of Computer Science and Software Engineering at Shenzhen University, Shenzhen, Guangdong, China. His research interests include deep learning, hyperspectral image classification, and



Yaqian Long received a Ph.D. degree from the University of Alberta, Edmonton, Canada, in 2019. She is currently an Assistant Professor with Shenzhen University, Shenzhen, China. Her study area is hyperspectral remote sensing in geological, ecological, and medical applications. Her primary research topic focuses on feature selection and classification using spectral mixture analysis and state-of-art machine learning techniques.



Rehan Ullah Khan received the B.Sc. and M.Sc. degrees in information systems from the University of Engineering and Technology at Peshawar, in 2004 and 2006, respectively, and the Ph.D. degree from the Vienna University of Technology, Austria, in 2011. He is currently an Associate Professor with the IT Department, CoC, Qassim University, Saudi Arabia. His current research interests include machine learning, segmentation, and image-based object recognition.



Irfan Ullah received the B.Sc. and M.Sc. degrees in electrical engineering from the Sarhad University of Science and Information Technology, Peshawar, Pakistan, in 2012 and 2015, respectively and in 2019, Ph.D. degree with the State Key Laboratory of Power Transmission Equipment and System Security and New Technology, School of Electrical Engineering, Chongqing University, Chongqing, China. In 2021, He has completed a Postdoctoral at the School of Engineering, Chulalongkorn University, Thailand.

He is currently working as an Associate Professor with the School of Computer Science, Chengdu University of Technology, China. He has published several papers in conferences and journals, such as IEEE Transactions on Power Electronics, IEEE Transactions on Magnetics, Applied Thermal Engineering, and IEEE Access.



issues on the Internet, IoT, and IoV.

Salabat Khan received his M.Sc and MS degrees both in Computer Science from the University of Peshawar and International Islamic University, Islamabad, Pakistan, respectively. He completed his Ph.D. degree in Computer Science and Technology from the Beijing Institute of Technology, Beijing, China. Currently, he is working as a Post-Doctoral fellow in the College of Computer Science and Software Engineering at Shenzhen University, Shenzhen, Guangdong, China. His main research includes machine learning, deep learning, security and privacy



Khalil Khan received the B.S. degree in electrical engineering and the M.S. degree in computer engineering from the University of Engineering and Technology, Peshawar, Pakistan, in 2007 and 2012, respectively, and the Ph.D. degree from the Signals and Communication laboratory, University of Brescia, Italy, in 2016. He is currently working as Assistant Professor in the department of Computer Science and Information Technology, Pak-Austria Fachhochschule: Institute of Applied Sciences and Technology, Pakistan.



Maqbool Khan (S'14, M'18, SM'22) is working as Assistant Professor at Pak-Austria Fachhochschule: Institute of Applied Sciences and Technology (PAF-IAST), Haripur, Pakistan and as Adjunct Researcher at Software Competence Center Hagenberg (SCCH), Austria. Recently he completed his Post-Doctorate from SCCH, Austria. Dr. Khan obtained a fully funded scholarship for his MS study at Huazhong University of Science and Technology (HUST) Wuhan and PhD study at Nanjing University in 2011 and 2013 respectively, awarded by China Scholarship Council (CSC) of China. He has multi-disciplinary expertise and working experience on diverse topics of Big Data Analytics, Cloud Computing, Predictive Maintenance, Explainable AI, Knowledge Graphs, Data Science and machine learning. He has more than 10-years of professional experience while working both in industry and academia. He worked in multinational companies like Siemens and Atos. Dr. Khan is a certified Google Cloud Professional Architect. He is an active researcher working on various projects with multiple collaborators and currently he is working on European Union project titled "Human-AI Teaming Platform for Maintaining and Evolving AI Systems in Manufacturing". He also won a project during Pakistan Scientific Foundation (PSF) CRP4 call as Principal Investigator..



Giovanni Pau (M'17) is an Associate Professor at the Faculty of Engineering and Architecture, Kore University of Enna, Italy. Prof. Pau received his Bachelor's degree in Telematic Engineering from the University of Catania, Italy, and both his Master's degree (cum Laude) in Telematic Engineering and Ph.D. from Kore University of Enna, Italy. Prof. Pau is the author/co-author of more than 80 refereed articles published in journals and conferences proceedings. He is a Member of the IEEE (Italy Section) and has been involved in the organization of several international conferences as a session co-chair and technical program committee member. Prof. Pau serves/served as a leading Guest Editor in special issues of several international journals and is an editorial board member as Associate Editor of IEEE Access, Wireless Networks (Springer), EURASIP Journal on Wireless Communications and Networking (Springer), Wireless Communications and Mobile Computing (Hindawi), and Future Internet (MDPI). His research interests include Wireless Sensor Networks, Fuzzy Logic Controllers, Intelligent Transportation Systems, Internet of Things, and Network Security.